Contents lists available at ScienceDirect

Extreme Mechanics Letters

Full range fragmentation simulation of nanoflake filler-matrix composite coatings on a polymer substrate

Cagan Diyaroglu [a,1], Rebecca Villanueva [a,1], Umar Raza [a], Selda Oterkus [b], Erkan Oterkus [b], Kyungjin Kim [a,*]

[a] *Laboratory for Advanced Manufacturing Reliability, Department of Mechanical Engineering, University of Connecticut (UConn), Storrs, CT 06269, USA*
[b] *PeriDynamics Research Centre, Department of Naval Architecture, Ocean and Marine Engineering, University of Strathclyde, 100 Montrose Street, Glasgow G4 0LZ, United Kingdom*

A B S T R A C T

This paper presents a comprehensive experimental and computational study to explore the damage evolution mechanisms of polymer matrix nanocomposite films consisting of rigid ceramic fillers coated on a polymer substrate. The weight ratio of montmorillonite (MMT) fillers in the polyvinyl alcohol (PVA) matrix ranges from 30 % to 70 %, and these are applied onto a polyethylene terephthalate (PET) substrate. Through experiments, apart from damage behaviors, the water vapor transmission rates are also measured to gain insight into moisture diffusion characteristics with varying weight ratios of fillers. The optimal weight ratio of nanocomposite films consisting of a PVA matrix with MMT fillers can vary depending on the purpose of damage resistance and moisture barrier characteristics. A peridynamic theory is employed to simulate various damage scenarios of bi-layer nanocomposite films. The solution strategy presented incorporates the use of the cut-boundary and finite element methods to reduce substrate thickness and make initial predictions of crack onset strains, respectively, under quasi-static loading conditions. Several damage scenarios are considered for thin and thick PVA films on the PET substrate, as well as weak to strong interfaces between the PET-PVA and PVA-MMT layers. Additionally, different distributions of MMT fillers are also considered by varying the distances between them and inserting inclusions. The peridynamic damage analyses encompass crack initiation, propagation, and final failure stages across a wide range of strains, including various damage modes such as matrix cracking, cracking at the filler-matrix, or matrix-substrate interfaces, leading to the cohesive film cracking and delamination.

1. Introduction

The polymer nanocomposite market has shown consistent growth in the recent decade [1] and extensive research has been conducted on inorganic filler – organic matrix nanocomposites, particularly focusing on their microstructure, gas and moisture diffusion barrier, and mechanical properties. Among inorganic fillers, flake-like two-dimensional (2D) nanomaterials such as clays, graphene, and graphene oxides serve as excellent nanosheet building blocks after exfoliation, creating a dense array of aligned platelets and/or multilayers that significantly increase the water molecule diffusion path in an organic polymer matrix. [2–8] Moisture barrier performance improves by controlling the filler content. [9–15] With alterations of filler and matrix concentrations, orientations [16], processing methods and treatments, [11,17–19] these

nanocomposite films can be further optimized to serve diverse applications such as gas barriers, [14,20–23] molecule separation, [24–26] moisture barriers, [9,10,12,13,15,27] flame retardant coatings [11, 28–30] for food processing, pharmaceutical, wearables and implantables, as well as battery applications. [31–33] Furthermore, substrate conditions induced during the processing and pre/post-processing, e.g., particle/void inclusions, [34] residual stresses, [35] surface roughness, [36] and surface treatments, [37] can alter the functionality of nanocomposite coatings themselves.

Montmorillonite (MMT) clay is the type of nanoflake widely utilized due to its ease of exfoliation and modification. [25] MMT consists of surface-substituted aluminosilicate layers, each approximately 1 nm thick, intercalated with metal cations and stacked into multilayer formations of 1 ~ 10 μm in size. By modifying the surface of clay layers

---

appropriately, MMT can be dispersed in a polymer matrix, resulting in the formation of polymer-clay nanocomposites. Moreover, organic modifiers can be used to treat MMT, enhancing its compatibility with matrix materials. [38] Individual clay layers of only a few nanometers thick become completely separated in the matrix and form exceptionally dense and highly aligned arrays. Meanwhile, polyethylene terephthalate (PET) is the most common polymer substrate available as a bulk film that not only the MMT and other nanoflakes (also called nanoplatelet arrays) but also ultrathin conformal metal oxide and nitride layers are coated on its surface. [2,21,24,35,39–43] PET is also used as the substrate for active layers of flexible organic electronics. [44–46] Nanoflake based thin film coatings can be advantageous for such applications that involve constant and repeated mechanical deformations throughout their shelf life due to their flexibility [47–49].

Although the elastic limit of inorganic thin film barrier coatings is typically limited to a crack onset strain (COS) of only a few percent (i.e., 1 – 3 %), it is adequate for rollable, bendable, and foldable electronics by preserving the integrity of the thin layer [35,39,50–52] and the substrate or carrier layer can be designed (e.g. serpentine, horseshoe curves) to increase the stretchability. [53–56] The increased density of rigid inorganic fillers such as MMTs in the organic polymer matrix leads to a comparative range of COS with conformal inorganic coatings. Understanding the onset of crack propagation and the resulting paths leading to failure is more complex than homogeneous inorganic coatings, which typically exhibit channel cracks across the entire width of the film. [57] Li et al. [58] investigated the fracture behavior of nanoscale laminated Si_3N_4/BN composites in which BN represents soft, weak interfaces between rigid Si_3N_4 layers. A higher Si_3N_4 content in BN interfacial layers makes the interfacial layers stronger and crack deflection more difficult, such that through-thickness cracking is dominant. In another study, Morits et al. [59] utilized nano-sized MMT clay and polyvinyl alcohol (PVA) polymer matrix nanocomposites to replicate the fracture toughness of nacre-inspired materials. Fracture testing showed crack deflection and fracture toughness of 3.4 MPa·$\sqrt{m}$, not far from nacre. Wang et al. [60] created layered MMT platelet/nano fibrillar cellulose (NFC)/PVA binary layered nanocomposites. They found MMT pull-out damage with fibrils fracture and crack bridging between the layers. Peng et al. [61] aimed to enhance the toughness of Polydimethylsiloxane (PDMS) by incorporating layered MMT, leading to a significant 12-fold improvement in toughness. Additionally, they investigated crack propagation paths during mode-I tensile testing and observed crack bridging and propagation between the layered MMTs perpendicular to the preexisting crack. Finally, Wang et al. [62] provides an overview of fracture mechanisms in layered nanocomposites that mimic nacre, consisting of 95 % inorganic and 5 % organic constituents by volume. The experiments revealed that the primary fracture modes are platelet pull-out and interfacial cracking between the layers, with some platelet fractures occurring at high volume fractions due to the flaws within ceramic fillers. The dominant interfacial fracture modes can also be observed in a review paper by Corni et al. [63] on laminated Si_3N_4-BN nanocomposites. Besides, another review paper by Bonderer et al. [64] demonstrates the impact of the aspect ratio of $CaCO_3$ and Al_2O_3 platelets on a fracture mode in a ductile polymer matrix. Higher aspect ratios tend to result in platelet fracture, while lower ratios lead to a platelet pullout mode.

Several researchers conducted computational studies to understand crack initiation sites and paths leading to the final failure of filler-matrix composites. In a study conducted by Ongaro et al. [65], the classical continuum mechanics theory and a peridynamics-based unit cell approach are combined to predict the effective tensile modulus and fracture toughness of polymer-based nanocomposites. In the PD model, the 1–5 wt% MMT clays of the epoxy matrix were represented as one-dimensional non-straight curved lines. They compared mode-I crack growths of bare polymer with those of polymer containing 3 wt% MMT fillers and observed a tortuous crack path in the clay-content polymer in contrast to the bare polymer, aligning with the findings from the

experimental tests. Lawrimore et al. [66] investigated the interface cracking behaviors of PVA matrix/MMT nanocomposites. They employed molecular dynamics simulations to determine interfacial fracture toughness values of PVA-MMT. These values were then integrated into finite element models based on the cohesive zone method. The models represented three-dimensional (3D) cylindrical forms of the intercalated lamellar structure of PVA matrix and 1 wt% MMT in a unit cell. Through this multi-scale approach, calibrated with experimental data, the researchers successfully captured interfacial crack propagations between the PVA matrix and MMT clays. Nayak et al. [67] utilized the peridynamic (PD) and cohesive zone-based finite element (FE) methods to simulate the damage paths of cementitious composites that involve 10–30 % metallic particulates within a unit cell. The computationally determined average Young's modulus, tensile strength, and fracture energy closely matched the experimental results. This study also demonstrates the alignment of FE results with PDs results and experiments. The findings highlight the effectiveness of the PD method over the cohesive zone-based FE method, as it requires fewer input parameters (i.e., critical stretch for crack initiation and propagation), and the crack paths are independent of FE meshes. Baber et al. [68] also investigated the incorporation of rigid carbon nanotube (CNT) yarns within a polymer matrix composite, a configuration that involves voids. The study considered the random distributions of CNTs and voids using probability density functions. Comparative studies show that PD theory can capture damage outcomes and stress-strain curves aligned with the results of experiments. In another study conducted by Jenabidehkordi et al. [69], the fracture behaviors of polymer matrix composites were investigated. The composites involved spherical inclusions with a volume ratio ranging from 0.2 % to 50 % and varying stiffness ratios compared to the polyethylene matrix, ranging from 2 to 1000. The analyses were performed on a rectangular unit cell, and the results, compared to experiments, were able to capture damaged paths. However, the study only considered single interface fracture toughness between the polymer matrix and the rigid particles.

The PD theory is structured as an extended version of classical continuum mechanics theory, exhibiting several benefits compared to other methods such as the finite element-based cohesive zone method. In the classical continuum mechanics (CCM) theory by Augustin Louis Cauchy, only neighboring interactions of an infinitesimal volume are considered with traction vectors. The PD theory further incorporates distant interactions in the most general sense. The length scale, termed as horizon, designates extent of such interactions and classical theory can be recovered as it approaches to zero. The most remarkable property of the PD theory is that the equation of motion does not include any spatial derivatives as in the CCM theory. As a result, the PD theory has several advantages over local theories. In the fracture mechanics sense, the PD theory is especially promising for failure analysis of structures because the formulation is valid everywhere regardless of the presence of discontinuities in the domain, and it does not require any external crack growth criteria to predict when and where the crack propagates. In simulating cracking behaviors of nano-fillers inside polymer matrix, the PD theory does not require any pre-cracks, and the cracks emerge and propagate spontaneously depending on the fracture toughness values of the polymer matrix, ceramic filers, and interfaces between them. The capability of the PD theory has been demonstrated by several researchers with many benchmark problems, and the advantages mentioned above are validated by experimental findings [70–74].

When filler-matrix nanocomposites are applied as barriers or functional coatings onto substrates, the combined filler-matrix-substrate failure modes address the mechanical durability of the targeted applications. Most studies involving thin coatings on the substrate focus on the homogeneous films and/or individual preexisting cracks to examine the crack growth and fracture behaviors [75–77] and it becomes an oversimplified assumption for filler-matrix nanocomposite films. The filler-matrix nanocomposite materials are statistically homogeneous at the macroscopic scale yet heterogeneous at the microscopic scale. The

fragmentation behavior shows highly localized crack growths around the onset of cracking. The origin of the localization appears to be different per processing-structure parameter and results in different fragmentation behaviors. Identifying the failure mode and damage evolution behavior of filler-matrix nanocomposite films on the compliant substrates under monotonic loading will likely assist in

improving the processing and structural designs, e.g., arresting cracks.

In this study, we conduct *in-situ* microscopy tensile fragmentation tests to observe damage evolution behaviors of flake filler-matrix nanocomposite films on a PET substrate. The nanocomposite films are comprised of MMT fillers of varying weight ratios in a PVA matrix. The weight ratio of MMT fillers inside the PVA matrix, in experiments, is
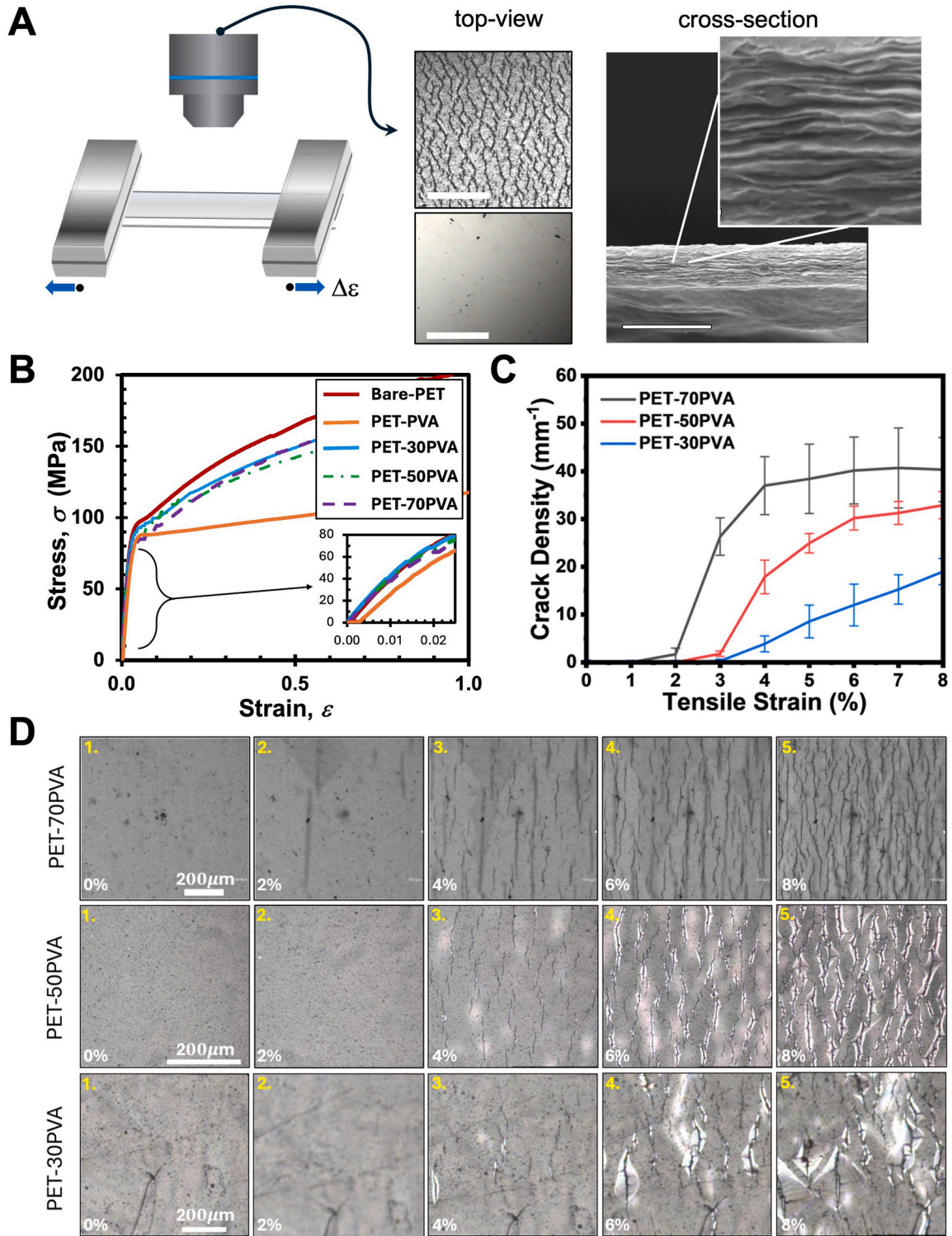
Fig. 1. Experimental characterization of nanoflake composites fragmentation behavior (A) a schematic image of in situ microscopy tensile test setup and in situ top-view optical image of 50 % MMT/PVA (top-left) and Bare-PVA (bottom-left) and cross-sectional scanning electron micrograph (right). Here, 30 dip coatings on PET substrates are used as example images. Scale bar: 100 μm (B) Engineering stress-strain curves of nanocomposite films. (C) Crack densities at different levels of applied strains with 30 %, 50 %, and 70 % MMT fillers. (D) The damage evolution behavior observed for PET-70PVA (top), PET-50PVA (middle), and PET-30PVA (bottom).

used as 30, 50 and 70 %. A dipping method is used to produce a natural flow-induced filler-matrix nanocomposite layers dissolved in a solution, followed by curing the aligned structure coated on PET. Following the experimental work, the computational study based on PD theory is conducted in order to investigate fracture behaviors of nanocomposite films with varying distributions of MMTs and the interfacial fracture toughness between the PVA matrix and MMT fillers as well as the PET substrate and PVA matrix. The PD theory is advantageous in simulating crack initiations and propagation paths from crack-free configurations due to its mathematical structure involving integro-differential equations, and the meshless method is advantageous over the finite element method that does not require any re-meshing or suffers from shear locking. Damage criteria for initiation and propagation are based on the material property of mode-I critical energy release rate. The computational study presented in this paper utilizes PD theory to assess experimental observations of COS and the propagation of cracks leading to the final failure (cracks at saturation) under tensile loadings.

As explained above, several computational studies have explored limited ranges of filler weight ratios, applied strains and/or single-layer nanocomposites without the substrate for the damage behaviors of nanocomposite films. This study aims to investigate critical failure modes and fracture behaviors of flake filler-matrix-substrate materials across a wide range of strains, including matrix cracking, cracking at the filler-matrix or matrix-substrate interfaces, leading to the cohesive film cracking and delamination. Additionally, the distance between fillers and interfacial fracture toughness are considered to help better design targeted applications based on organic polymer substrates in combination with filler-matrix barrier coatings.

2. Experimental results

Experimental characterization on the fragmentation behavior of MMT/PVA-PET samples are shown in Fig. 1. The *in situ* microscopy tensile test allows a continuous monitoring of top-view optical images under the monotonic increase of applied strains for MMT/PVA films, containing dense MMT filler arrays as shown in the cross-sectional images of 30-dips MMT/PVA and Bare-PVA on PET (Fig. 1A). The thickness of coatings ranges between ~40 and ~45 mm for 30 dips and ~14 mm for 10 dips. The effect of plasma treatment slightly increases the thickness by less than 1 mm per 10 dips. The stress-strain curve of PET substrates with and without MMT/PVA coatings is shown in Fig. 1B. The MMT/PVA coatings composed of MMT filler materials at weight ratios of 0, 30, 50, and 70 % are indicated as PET-PVA, PET-30PVA, PET-50PVA, and PET-70PVA, respectively. Please also note that the weight ratios of MMTs inside the PVA matrix are related to the volume ratios of 0, 17, 32, and 52 %, respectively. The addition of a PVA layer onto a PET substrate significantly increases the ductility of the specimen compared to the bare PET (ultimate strains of 181 % vs. 110 %), while MMT fillers inserted at different weight ratios into the PVA matrix decrease the ductility, back to the bare PET's (88.5 ~ 113 %) due to the high elastic modulus of MMTs. The hardening behavior of the PET-XPVA nanocomposites varies with the emergence of localized cracks and/or their evolutions within the PVA matrix. The ultimate strain decreases after reaching a 50 % MMT filler weight ratio. The average Young's moduli are found to be 3.15, 2.87, 3.20, 3.80, and 3.96 GPa for Bare-PET, PET-PVA, PET-30PVA, PET-50PVA and PET-70PVA, respectively. The modulus value increases with higher clay loadings. The PET-PVA sample exhibits a reduction in Young's modulus compared to the bare PET, attributed to the lower modulus of PVA, i.e., 2.75 GPa. [78] In addition to the PET and PVA properties, Manevitch and Rutledge [79] used the molecular dynamics method to analyze Young's modulus of a single MMT lamella and found approximately 270 GPa.

Crack densities are measured during the monotonic stretching of PET-30PVA, PET-50PVA, and PET-70PVA (Fig. 1C). The cracks that emerge through the length of the specimen are counted and averaged along its width within the intervals of 128 µm. The final value, named

crack density, demonstrates the number of cracks per unit length (mm) of the specimen. The COS values are observed to be 3.2 %, 2.9 % and 1.9 % for PET-30PVA, PET-50PVA, and PET-70PVA, respectively, decreasing as the MMT content increases. It is also worth noting that the PET-PVA nanocomposite (without MMT fillers) does not exhibit any localized cracks, as shown in Fig. 1A, until it reaches the ultimate strain of 181 %, indicating that the MMT fillers cause initiation and propagation of cracks. According to in-situ images in Fig. 1D, localized microcracks appear in all samples at the COS levels. As the strain increases, the local cracks disperse across the surface of the film, ultimately leading to an increase in crack densities. The crack densities of PET-70PVA increase significantly compared to other samples', reaching a saturation level of 40 per mm at nearly a 2.1 % strain increase after the COS. On the other hand, the crack density increasing speeds for PET-30 PVA and PET-50PVA are slower. PET-30PVA and PET-50PVA reach saturation after the emergence of initial cracks, nearly after 4.8 % and 4.1 % strain levels, respectively. The rapid development of localized cracks in PET-70PVA is evident in the in-situ images, which is attributed to the arrestment of cracks before reaching the PET-PVA interface as opposed to lower filler content films, i.e. PET-30PVA and PET-50PVA nanocomposite films. The schematics in Fig. 2A show such reasoning for low versus high filler loading composites, allowing increased delamination paths in lower filler loading composites. Similar microcracks observed in the 70 % and 50 % weight ratio of MMT fillers at 4 % strain turn into a higher density of localized cohesive film cracking and interfacial delamination, respectively, at 6 ~ 8 % strains. The PET-30PVA samples show more localized cracks than PET-70PVA and PET-50PVA, likely due to higher PVA portions across the farther gaps between MMT fillers.

Effect of plasma treatment and number of dipping layers on the damage evolution behavior are clearly shown in the image of PET-50PVA at the crack density saturation (Fig. 2B). Here, we would like to mention that the images shown in Figs. 1D and 2B for PET-50PVA without the plasma treatment have different cracking behaviors. Both samples are produced with the same conditions but have distinct features in crack bridging, which is the straight horizontal cracks between the vertical cohesive cracks. In Fig. 1D, the discrete and wavy cracks are observed at 8 % strain; however, in Fig. 2B, the continuous and straight cracks are developed. Even though both 50 % filler coatings are produced under the same conditions, they reveal different features in crack bridging. One possibility of the absence of crack bridging in Fig. 2B could be attributed to the environmental conditions during the barrier dipping coating process that affect the film-substrate interfacial bonding. The varying localization of exfoliated filler chunks and differing interfacial fracture toughness values between the filler-matrix and the film-substrate may explain this discrepancy. Nevertheless, we observed overall delamination, COS, and crack density behaviors of the 50 % coating are consistent and different from those of 30 % and 70 % coatings. Increased interfacial adhesion after the plasma treatment between the layers leads to continuous cohesive crack growths in the filler-matrix film layers without delamination from the substrate, and the increased thickness in 30 dips PET-50PVA reduces COS to half of 10 dips' COS, following the $1/\sqrt{thickness}$ trend when the proportional thickness increase is assumed for the number of dips (Fig. 2C). [21,80] The barrier improvement factor (BIF) of 10 dips and 30 dips PET-50PVA compared to the bare-PET in the same plot shows about a three-fold increased BIF ($\times$ 3.41) for 30 dips PET-50PVA, presumably coming from three times increased diffusion pathways. X-ray diffraction (XRD) analysis presents the crystal size of PET, PET-30PVA, PET-50PVA and PET-70PVA (Fig. 2D). While the most prominent peak per each sample reflects the presence of the PET substrate (Figs. S1, $2\theta \approx 26°$), as MMT wt % increases, a smaller peak appears at $2\theta \approx 7° \sim 9°$ and increases continuously, indicating the increasing presence of MMT crystals in the overall samples.

The effect of adding MMT flake fillers in the PVA matrix on the
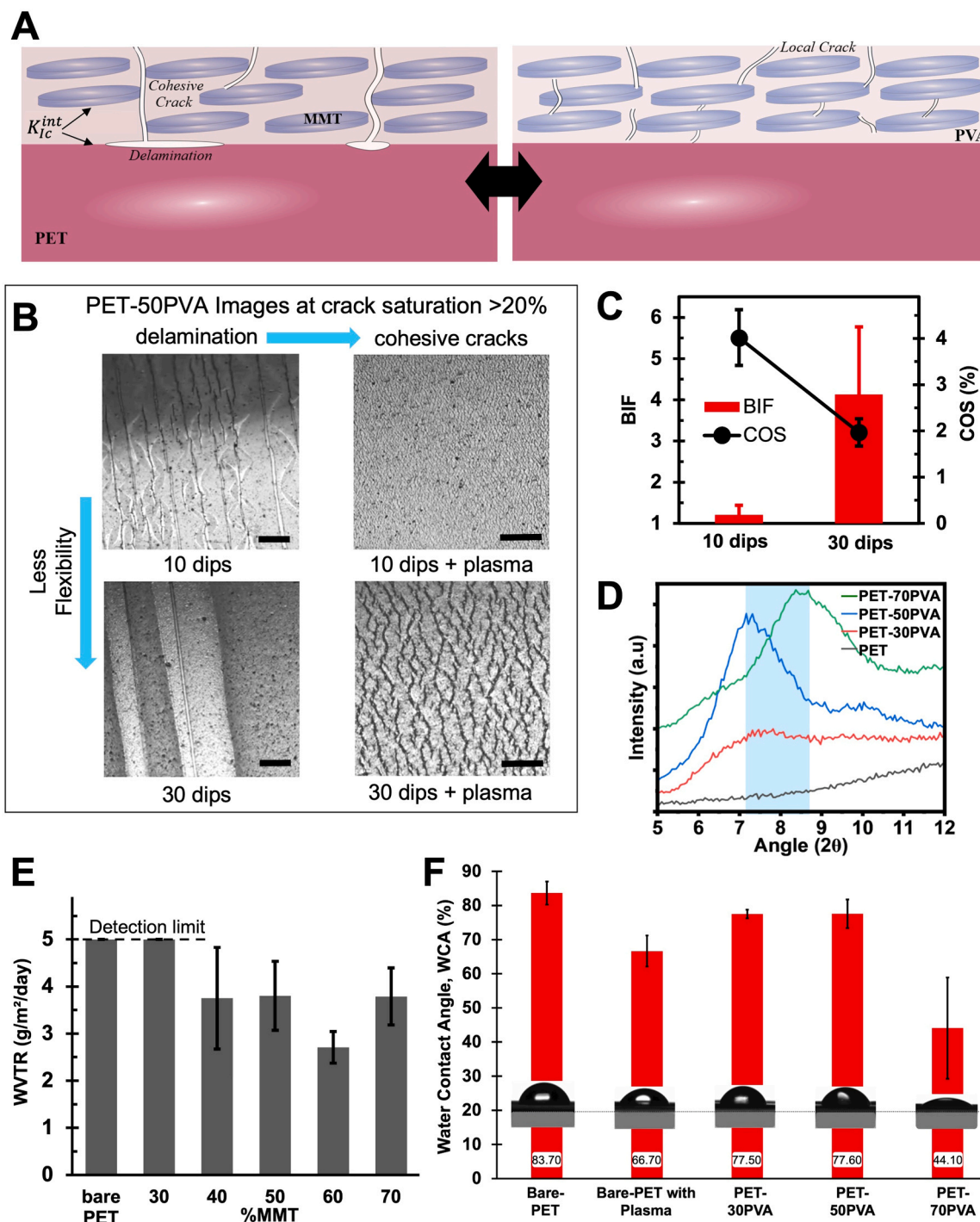
Fig. 2. Filler distribution and weight ratio effects on mechanical and barrier performances: (A) Schematics of cohesive cracks leading to delamination for lower filler loading (left) versus arrested localized microcracks for higher filler loading (right). (B) Crack damage evolutions at saturation of PET-50PVA, Scale bar: 50 μm. (C) The barrier improvement factor (BIF) and crack onset strain (COS) of 10 vs. 30 dips samples. (D) X-ray diffraction (XRD) analysis of bare PET and PETs coated with MMTs. (E) Water vapor transmission rates (WVTR) and (F) water contact angles (WCA) as MMT wt% increases.

moisture diffusion barrier performance is shown in Fig. 2E. The MMT filler loading from 0 % (bare PET) and 30 % to 40, 50, 60, 70 % shows a very mild improvement in water vapor transmission rates (WVTRs) for 10 dips coatings. The values stay the same order of magnitude at the testing condition (relative humidity (RH) 100 %, 37°C) for all ranges of the filler loading unless changes are made in the testing or processing conditions. For example, WVTRs of the 50 % filler loading decreases to 1.08 and 0.756 g/m²/day in 25 %RH and 30 dips coatings, respectively. The water contact angle (WCA) is measured to test an additional factor

that affects barrier quality (Fig. 2F). WCAs show how the film surface interacts with water droplets, indicating the film surface's water sorption tendency. [81] A film is described as hydrophilic or hydrophobic based on whether it has low or high water contact angles, respectively. The hydrophobic surface delays the sorption and can visibly decrease WVTR levels. [82,83] The increased hydrophilicity in PET-70PVA compared to ones in all other samples (including the surface plasma treated PET) is likely one of the reasons why WVTR increases after 60 % filler loading. These findings align with expectations, given MMT's

known water sorption properties and the ability of plasma treatment enhancing the surface adhesion.

3. Modeling results

We further investigate the damage characteristics of flake-filler-matrix composites from crack initiation to final failure, i.e., crack
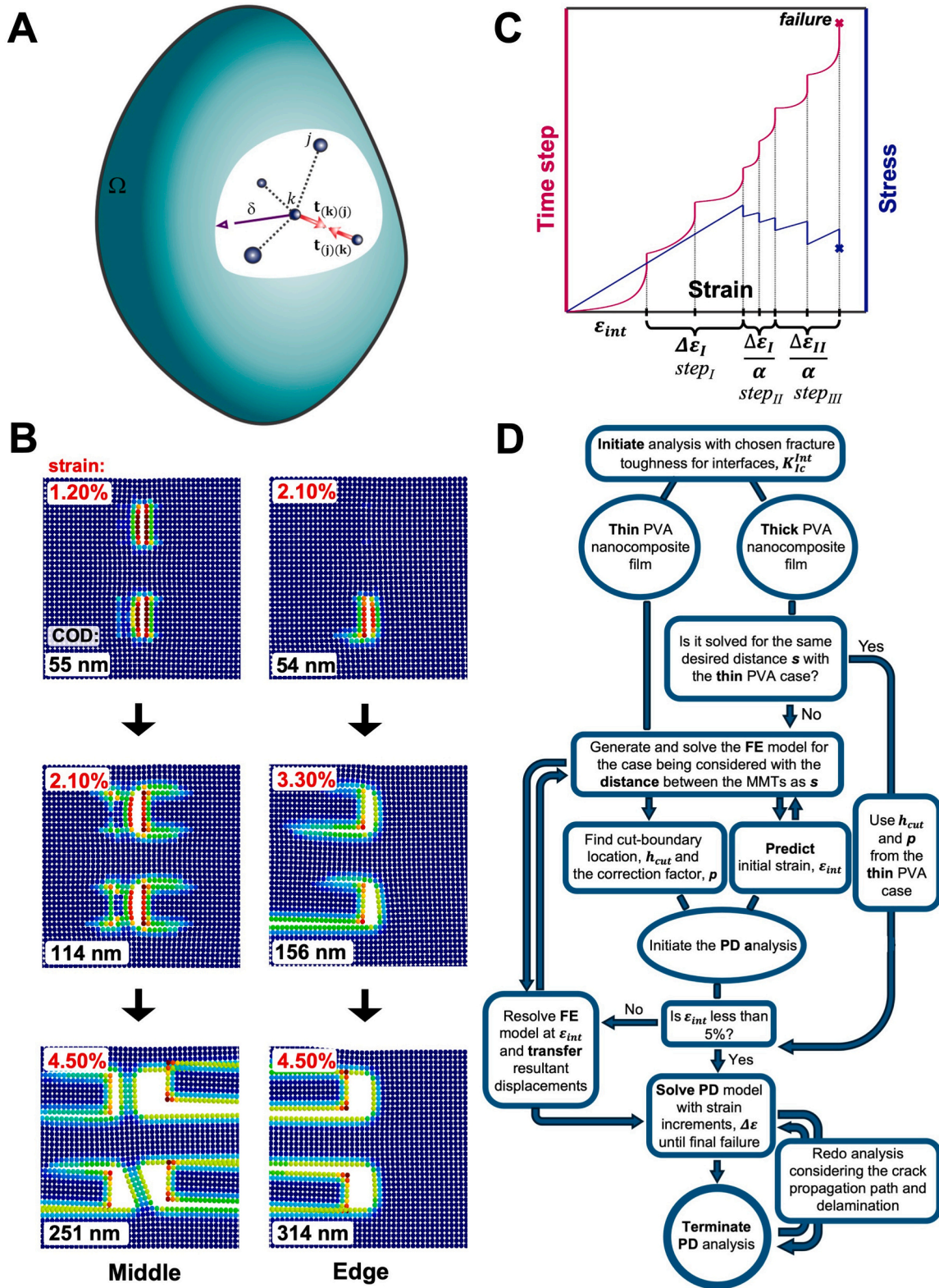
Fig. 3. Combined finite element (FE) and peridynamic (PD) modeling approach and solution strategy: (A) interactions within a deformed body, Ω (B) Simulation images of damage initiations at MMT-PVA interfaces from crack-free PD system; crack opening displacements (COD) and crack onset strains (COS) are indicated. The solution strategies to solve PD model with strain increment, shown as (C) a schematic plot and (D) overall flow chart.

density at saturation, using PD theory. The MMT fillers modeled in either finite element method or peridynamic theory have constant geometrical parameters. Exfoliation levels provided by Sigma Aldrich Inc and references [3] are applied, i.e. the thickness of 400 nm and diameter of 10 μm. The modeled cylindrical MMT particles are detailed in Section **S3.1**. Several scenarios are considered to understand damage behaviors. These include MMT distributions and fracture toughness values for the interfaces between MMT-PVA within the PVA matrix and the PET-PVA. Additionally, the FE method is utilized for the modeling and analysis of displacements and stress distributions within the thin films augmented with MMT fillers. All peridynamic analyses are performed using the adaptive dynamic relaxation (ADR) method to analyze crack propagation under quasi-static loading, representing experimental conditions. In some cases, where the crack emergence strains are higher, the displacements already found are transferred from the FE to the PD model in order to reduce computational time. Another type of improvement is achieved through less complex substrate modeling. This is done by comparing the FE results with classical continuum mechanics theory under plane strain conditions. The thickness of the PET substrate is reduced based on the MMT filler distributions outlined in the following sections. Computational improvements enable us to compute numerous scenarios in a short time, thus expanding our comprehension of the damage behavior of these nanocomposite films under increasing strains.

The flake fillers/matrix-substrate (MMT/PVA-PET) structure is analyzed using PD theory to verify converged displacement results without allowing any damage, and then the results are compared with FE method. Another reason for this verification is to track the convergence of the ADR method and determine the most efficient mass factors over time. The following section addresses various damage scenarios by comparing crack initiations, propagations, and final failures for different distributions of MMT while varying fracture toughness values for PVA-MMT and PET-PVA interfaces.

3.1. Theory

During peridynamic theory development, Kilic [84] utilized the ADR method for the first time, solving the dynamic form of the equation of motion given below statically.

$$\rho_{(k)}\ddot{\mathbf{u}}_{(k)} = \mathbf{F}_{(k)} \tag{3.1}$$

where ρ represents the material density, $\mathbf{u}$ and $\mathbf{F}$ are the displacement and force vectors, respectively. Moreover, the dots on $\mathbf{u}$ denote time derivatives. The force vector acting on a main material point k can also be explicitly depicted as:

$$\mathbf{F}_{(k)} = \sum_{j=1}^{N} \left(\mathbf{t}_{(k)(j)} - \mathbf{t}_{(j)(k)} \right) V_{(j)} + \mathbf{b}_{(k)} \tag{3.2}$$

The symbols $\mathbf{t}$ and $\mathbf{b}$ denote the force density and body load vectors here, while V represents each node's material volume. The summation encompasses all material points within the main material point's horizon $\delta_{(k)}$, as illustrated in Fig. 3A. It ranges from one to the total number of material points in a family of k, which is N.

The force density vectors acting on material points k and j are oriented in opposite directions and have equal magnitudes. These vectors are specifically aligned to satisfy both linear and angular momentums within a body and are designated as:

$$\mathbf{t}_{(k)(j)} = -\mathbf{t}_{(j)(k)} \tag{3.3}$$

$$\mathbf{t}_{(k)(j)} = \frac{1}{2} c s_{(k)(j)} \frac{\left(\mathbf{y}_{(j)} - \mathbf{y}_{(k)} \right)}{\left| \mathbf{y}_{(j)} - \mathbf{y}_{(k)} \right|} M_{(k)(j)} \tag{3.4}$$

in which c is the material property parameter named as the bond

constant, and s is the stretch of a bond given as:

$$s_{(k)(j)} = \frac{\left| \mathbf{y}_{(j)} - \mathbf{y}_{(k)} \right| - \left| \mathbf{x}_{(j)} - \mathbf{x}_{(k)} \right|}{\left| \mathbf{x}_{(j)} - \mathbf{x}_{(k)} \right|} \tag{3.5}$$

Here, $\mathbf{x}$ and $\mathbf{y}$ represent the reference and deformed position vectors of the material points, either k or j. The representation of damage in peridynamic theory is quite straightforward and does not lead to any singularities like in classical theories. This is because the failure parameter $M_{(k)(j)}$ within the summation function is not differentiated, and it can be explained as:

$$M_{(k)(j)} = \begin{cases} 1 & \text{if } s_{(k)(j)} < s_c \\ 0 & \text{otherwise} \end{cases} \tag{3.6}$$

This means that it is a step function, and the termination of interaction between the material points occurs when it equals zero, a process called bond breakage. The damage of each material point is defined as the ratio of the number of broken interactions to the total amount of interactions as:

$$\Phi_{(k)} = 1 - \frac{\sum_{j=1}^{N} M_{(k)(j)} V_{(j)}}{\sum_{j=1}^{N} V_{(j)}} \tag{3.7}$$

Near the crack openings, the damage parameter $\Phi_{(k)}$ ranges between 0.25 and 0.5. The critical stretch parameter in Eq. (3.6) is defined as [70]:

$$s_c = 2\sqrt{\frac{G_c}{c\delta^4}} \tag{3.8}$$

where G_c is the critical energy release rate (fracture energy) which is a material property, and bond constant under plane strain condition can be derived as [71,72]:

$$c = \frac{24\mu}{\pi\delta^3} \tag{3.9}$$

The shear modulus here is defined as $\mu = 2E/5$ under conditions of constant Poisson's ratio $1/4$. This is a requirement of the peridynamic theory for the computational analyses presented in this section.

In the ADR method, the left-hand side of Eq. (3.1) is replaced with the fictitious parameters of diagonal density matrix ($\mathbf{D}$) and damping coefficient (c_d) as below.

$$\mathbf{D}\ddot{\mathbf{u}} + c_d\mathbf{D}\dot{\mathbf{u}} = \mathbf{F} \tag{3.10}$$

Solving the above equation over time leaves us with only the static equation of $\mathbf{F}$. The diagonal elements (λ_{kk}) of the $\mathbf{D}$ matrix can be determined utilizing the formula of

$$\lambda_{kk} = \frac{c}{4} m \sum_{j=1}^{N} \frac{\left| \left(\mathbf{x}_{(j)} - \mathbf{x}_{(k)} \right) \cdot \mathbf{e} \right|}{\left| \mathbf{x}_{(j)} - \mathbf{x}_{(k)} \right|^2} V_{(j)} \tag{3.11}$$

where $\mathbf{e}$ is the unit vector along the x and y directions, and m denotes a mass correction factor that should be determined for efficient convergence times. The dynamic equation given in Eq. (3.10) converges to the stable static equation given in Eq. (3.1). This convergence is achieved by choosing the effective damping coefficient c_d which could be considered as the most crucial part of the ADR method. The most effective value of c_d during analysis can be calculated from the lowest frequency, ω_0, of the system as:

$$c_d = 2\omega_0 \tag{3.12}$$

and

$$\omega_0 = \sqrt{\frac{(\mathbf{u^n})^T \mathbf{K^n} \mathbf{u^n}}{(\mathbf{u^n})^T \mathbf{u^n}}} \tag{3.13}$$

in which the superscript n and T indicate the time step number and

K^n is the diagonal stiffness matrix which is defined as

$$K^n = \frac{\frac{F^n}{\lambda_{kk}} - \frac{F^{n-1}}{\lambda_{kk}}}{\Delta t} \frac{1}{\ddot{u}^{n-1/2}} \tag{3.14}$$

where Δt denotes the time step size. The displacement and velocity vectors are integrated between the times steps by using explicit central – difference time integration technique. The details of the ADR method and the calculation of the adaptive damping coefficient, which effectively deactivates the dynamic part of the equation of motion, can be found in the reference 84.

3.2. Analyzing the behavior of nanocomposite films under quasi-static loading

It is possible to predict COS by comparing von Mises stresses at the tip locations of the MMTs. The strain just below the predicted COS in the FE model could be utilized as an initial strain for the PD damage analysis. The maximum stresses are concentrated within the MMT fillers; however, they are quite rigid, and the stress levels are significantly below the threshold for fracture. The stress concentrates on the MMT tips and the maximum levels are observed at the bottom tips as 16.47×10^{-4} and 16.33×10^{-4} N/μm² for thin and thick PVAs, respectively. Simulations without damage and our solution strategies are explained in **Section S3** of supporting information in detail.

The PD theory involves the analysis of crack initiation, propagation, and final failure achieved by incremental strains and the solution of the model with the ADR method at each step in a quasi-static manner. Fig. 3**B** shows the example crack initiations and propagations simulated for PET-30PVA in the PD system. The tensile strain ε_x applied to the right edge of the nanocomposite film is expressed as

$$\varepsilon_x = \varepsilon_{int} + \Delta\varepsilon_I \left(step_I + \frac{step_{II}}{\alpha} \right) + \Delta\varepsilon_{II} \frac{step_{III}}{\alpha} \tag{3.15}$$

where $\Delta\varepsilon_I$ and $\Delta\varepsilon_{II}$ denote the strain increments after crack initiation and at later stages after delamination initiation at the PET-PVA interface, respectively. The second strain increment $\Delta\varepsilon_{II}$ is typically characterized by its size, which is larger than the $\Delta\varepsilon_I$, as delamination damage at the PET-PVA interface propagates slower than cracks inside the PVA matrix. In Eq. (3.15), once the damage is detected with levels exceeding 0.10, the number of strain increments counted by $step_I$ is deactivated, and $step_{II}$ begins, while counting the number of strain increments until the $step_{III}$ and crack propagation analysis terminates upon cracks reaching the film surface, which is identified as the final failure. Here, the parameter α ensures that the strain increments after the crack initiates are smaller than the increment before initiation and it is usually chosen to be between 5 and 10. While implementing the ADR method in PDs, the strains are incrementally increased over fictitious time steps, as shown in Fig. 3**C** by pink solid line. After each increment, the ADR method continues by applying fixed strains to allow breakage of the peridynamic bonds. If any bond is broken during this phase, the time steps continue until the displacements converge, followed by a strain increment. However, no bond breakage is allowed during the strain increments.

Regarding the convergence criteria, the error is determined using the Euclidean norm as

$$\in_Q = \frac{\sqrt{\sum_{k=1}^{M} (Q - Q')^2}}{\sqrt{\sum_{k=1}^{M} Q^2}} < 10^{-8} \tag{3.16}$$

in which Q represents the displacements in the x and y directions, i.e. U and V, respectively. The quotation symbol denotes the displacements from the previous time step, and M is the total number of peridynamic material points inside the body, Ω. If the condition specified in Eq. (3.16)

is satisfied with either $\in_U$ or $\in_V$, the cumulative error is then calculated over 10,000 time steps by

$$E_Q = \sum_{T=1}^{10,000} \frac{\in_Q + \in'_Q}{2} < 4 \times 10^{-3} \tag{3.17}$$

for the x and y displacements. The ADR steps are considered to have converged when the E_Q is less than 4×10^{-3} for both U and V.

A flow chart shown in Fig. 3**D** outlines the solution strategies discussed above for the analysis of nanocomposite films with thin and thick PVAs. It is also considered here the varying distance between the MMT fillers (s) for examining damage behavior from crack initiation to failure.

3.3. Damage evolution behavior

We focus on the three damage types within the peridynamic bond: matrix cracking and interfacial cracking between MMT-PVA and PVA-PET crossing dissimilar materials. We assume the absence of cracking within the MMT fillers and PET substrate because of the pre-cracked nature of the flake fillers compared to homogeneous brittle film layers and the observed fragmentation images during the experiment carried out, respectively. Geometrically, two cases of filler-matrix film thicknesses are considered for MMT/PVA-PET: thin and thick PVA films deposited onto the PET substrate. The thicknesses of PET substrate, thin and thick PVA films are chosen as $h_{pt} = 65.50$ μm (half thickness from the line of symmetry), $h_{pv}^{Tn} = 1.80$ μm and $h_{pv}^{Tk} = 14.40$ μm, respectively, that align with experimental measurements. The geometrical dimensions of all films including the unit cell dimensions are detailed in **Section S3** with representative figures.

For the simulations of MMT/PVA-PET for various damage scenarios using peridynamic theory, a damage criterion outlined in Eq. (3.6 and 7) is employed. This criterion allows the failure parameter $M_{(k)(j)}$ to be either null or one, depending on the critical stretch parameter value, i.e. s_c. The interaction between material points terminates if its stretch value is less than the critical stretch of a bond, or in general terms, a peridynamic bond breaks. Here, the critical energy release rate (G_c) plays a crucial role in the critical stretch parameter, determining the initiation and propagation of cracks along with the final failure damage at saturation within the material and its interfaces.

Bond breakages within the PVA film and interfaces between PVA-MMT and PVA-PET are allowed with the fracture toughness values of PVA and interfaces denoted as K_{Ic}^{PVA} and K_{Ic}^{Int}, respectively. In PD theory, each bond is explicitly defined with these parameters in determining the critical stretch. The average fracture toughness is utilized for the PVA matrix, i.e. $K_{Ic}^{PVA} = 1.0$ MPa$\sqrt{\text{m}}$, [59,76,73] and the interfacial fracture toughness value (K_{Ic}^{Int}) ranged between 0.1 and 1.0 MPa$\sqrt{\text{m}}$, is investigated to reflect its dependency on the specific bonding characteristics exhibited between the different materials, as well as to match with experimental results.

Interfaces are typically treated by using a geometric average of the material parameters in PD theory [74] associated with the peridynamic bond. In this context, this parameter is the equivalent shear modulus calculated by

$$\mu_{(k)(j)} = \frac{\sum_{m=1}^{N_m} l_m}{\sum_{m=1}^{N_m} \frac{l_m}{\mu_m}} \tag{3.14}$$

where N_m denotes the total number of bond segments (l_m) that crosses different types of materials and μ_m is the shear modulus of each segment, i.e. $\mu_m = 2E_m/5$, as depicted in Fig. 4**A**. Moreover, the equivalent bond constant $c_{(k)(j)}$ can be determined by substituting $\mu_{(k)(j)}$ into Eq. (3.8). Taking into account the critical stretch parameter (s_c) denoted in Eq. (3.7), the $c_{(k)(j)}$ has a profound impact on it. In order to investigate this
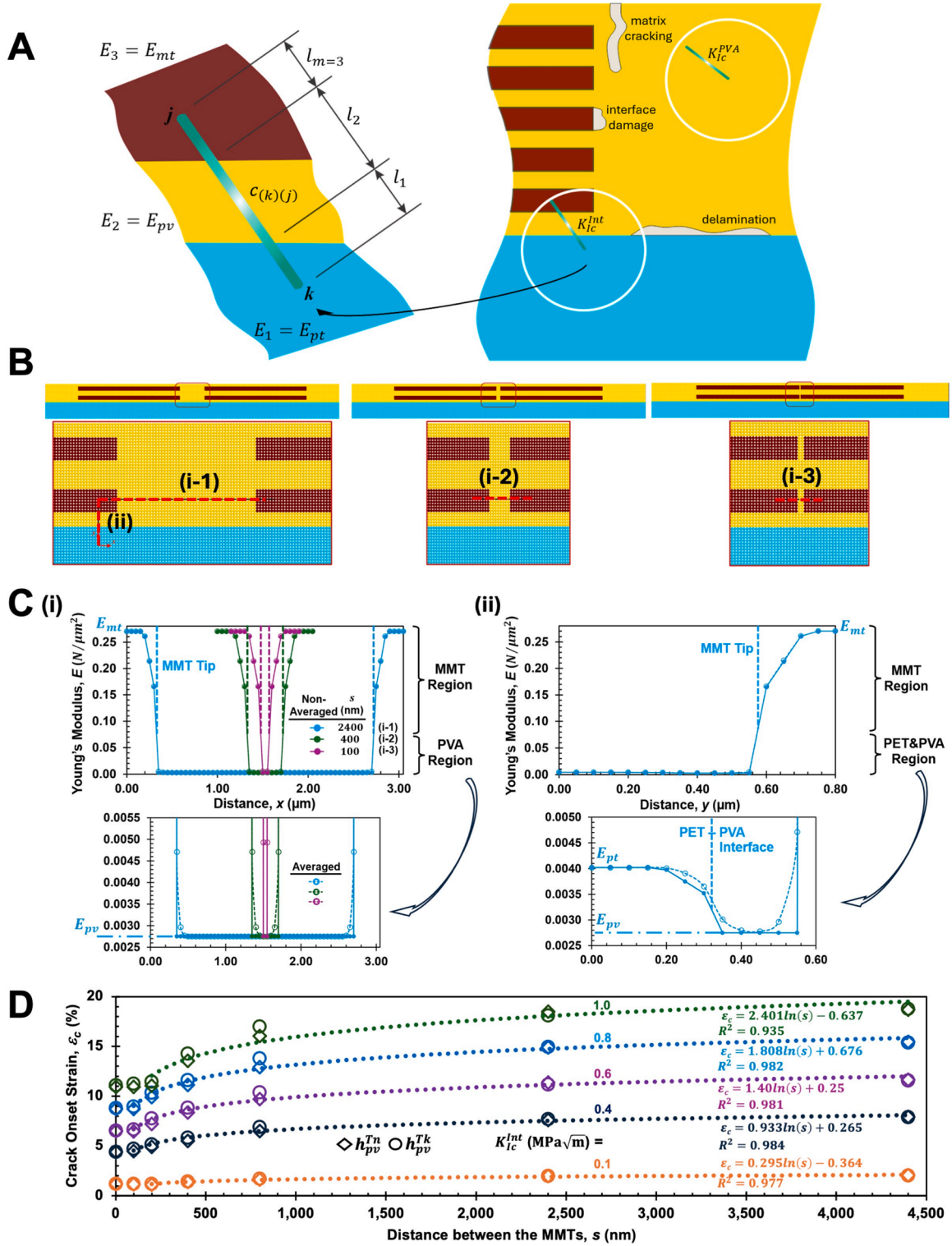
Fig. 4. Damage types and effect of distance between MMTs on COS: (A) The damage types within the PVA matrix and peridynamic bond crossing dissimilar materials. (B) MMTs in PVA matrix at varying distances, s, 2400 nm 400 nm, 100 m from left to right. (C) The average Young's modulus of material points near interfaces located on the dashed lines in (B). (D) The change in COSs as the distance between the MMTs increases for different interfacial fracture toughness, K_{Ic}^{int}.

impact near interfaces, the average Young's modulus at each material point is calculated by

$$E_{(k)} = \frac{5\pi\delta^3}{48} \sum_{j=1}^{N} c_{(k)(j)} \qquad (3.15)$$

Using the above formula for material points near the PET, PVA, and

MMT interfaces, $E_{(k)}$ is plotted for the cases of varying distances (s) between the MMTs. Fig. 4**B** shows the thin film cases with various distances between the MMT fillers, $s = 2400, 400, 100$ nm. The average Young's modulus of material points located on the dashed lines (in Fig. 4**B**; (i-1), (i-2), (i-3), (ii)) is presented in Fig. 4**C**. It shows the non-averaged Young's modulus derived from the bond constant by

employing an equivalent shear modulus described in Eq. (3.14) as equal to the shear modulus of the PVA matrix, i.e. $\mu_{(k)(j)} = \mu_{pv}$, specifically for the interface bonds depicted with solid lines. As shown in Fig. 4C (i), Young's modulus of MMT points near the interfaces gradually decreased in the order of 0.6. Conversely, Young's modulus of PVA points increased by a factor of 1.7, making the points even stiffer than the PET substrate between the MMT fillers. Moreover, for closer MMTs ($s =$

100 nm), the only calculated Young's modulus for the material points between the MMTs is 4.93 GPa, which is 1.8 times stiffer than the original PVA matrix. With regard to the PET-PVA interface (Fig. 4C (ii)), there is a minimal difference between the averaged and non-averaged Young's modulus at material points near the interfaces because of the closer elasticity modulus of PET and PVA. The substantial difference in elasticity between MMT and PVA results in a significantly greater effect

Fig. 5. The PD all stage damage results for (A) crack initiation, (B) propagation, and (C) final failure at saturation with varying interfacial fracture toughness and distances between the MMTs.

on interface stiffnesses, which consequently influences the bond constants. Considering the critical stretch parameter calculated by Eq. (3.7), its value can decrease by as much as 1.34, given the relationship between them as $s_c^{PVA} = \sqrt{1.8} s_c^{Int}$. Hence, Eq. (3.14) is exclusively applied for PET-PVA interfaces, and for MMT-PVA interfaces, the equation reduces to $\mu_{(k)(j)} = \mu_{pv}$. By doing this, the critical stretch parameter is not affected by the stiffness of the MMT fillers but is affected by the μ_{pv} as well as the fracture toughness of the interfaces; $s_c^{Int} \sim K_{Ic}^{Int}/E_{pv}$. Please also note that the critical energy release rate can be calculated by
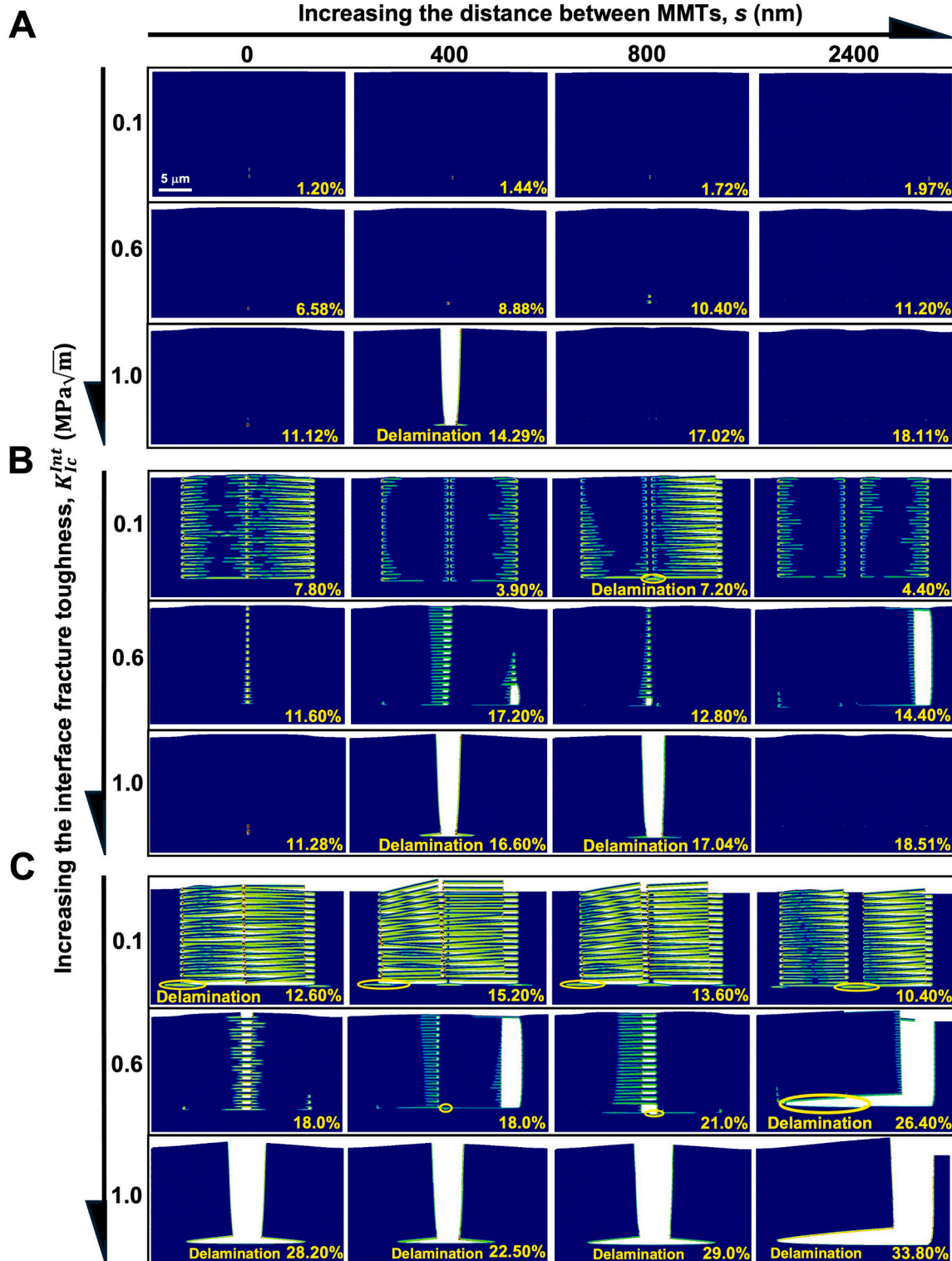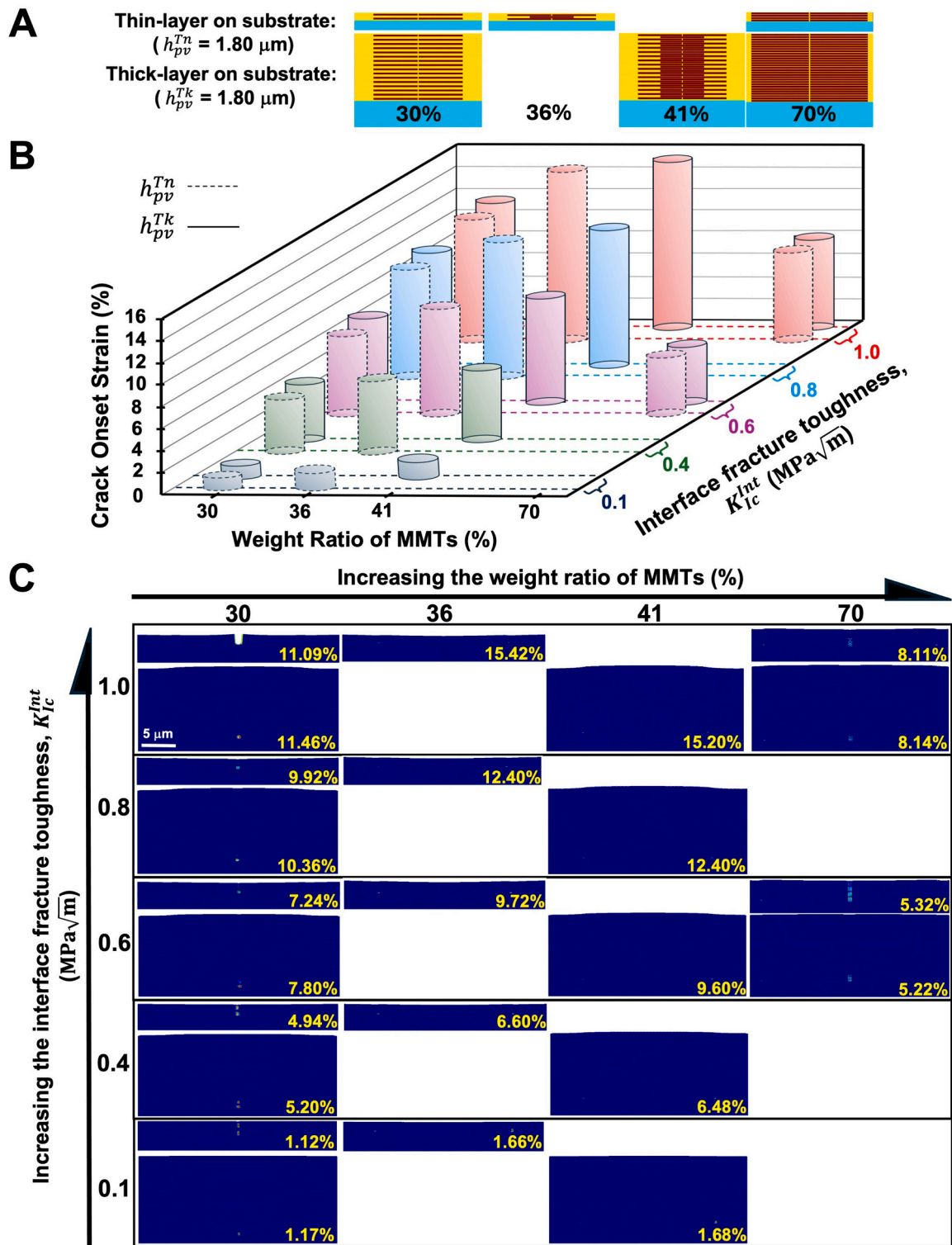
$$G_c = \frac{K_{Ic}^2}{E'} \tag{3.16}$$

to be used in the critical stretch parameter formula (Eq. (3.7)) and $E' = E/(1 - \nu^2)$.

Various damage scenarios are analyzed for varying distances between the MMTs, i.e. $s = 0, 100, 200, 400, 800, 2400$ and 4400 nm, and different values of interface fracture toughness, i.e. $K_{Ic}^{Int} = 0.1, 0.4,$ $0.6, 0.8$ and 1.0 MPa$\sqrt{\text{m}}$ between the PVA-MMT and PVA-PET interfaces. Besides, the thin (h_{pv}^{Tn}) and thick (h_{pv}^{Tk}) PVA films deposited onto the PET substrate are considered in the analyses. It is also important to note that the fracture toughness of the PVA matrix (K_{Ic}^{PVA}) is fixed at a defined value of 1.0 MPa$\sqrt{\text{m}}$, as discussed in the previous section. All the results of the peridynamic damage analyses for each scenario solved can be found in **Section S4**.

Fig. 4D depicts the COS for each K_{Ic}^{Int} case while altering the distance between the MMTs from $s_{\min} = 0$ to $s_{\max} = 4400$ nm. It is evident from the figure that COS decreases as the distance s decreases. In each case, with a specific K_{Ic}^{Int} value, the maximum COS ($COS_{\max}$) is found at the $s_{\max}$, and the minimum COS ($COS_{\min}$) is found at either or both the $s_{\min}$ and $s = 100$ nm. For all cases, the ratio of $COS_{\min}$ to $COS_{\max}$ is calculated to be between $55 - 59$ %, with specific values provided as; 59.113 %, 55.95 %, 57.59 %, 57.48 % and 59.15 % for $K_{Ic}^{Int} = 0.1, 0.4, 0.6,$ 0.8 and 1.0 MPa$\sqrt{\text{m}}$, respectively. The differences between the COS for the thin and thick PVA cases are mostly negligible. However, a significant difference is observed when the $s = 400$ and 800 nm, with the COS of the thick PVA being slightly larger than the COS of the thin PVA. In the figure, the best curve fit equations based on the least squares minimization method are also provided to demonstrate the average change in the COS with the distance s.

Fig. 5 demonstrates the PD results for the stages of crack initiation, propagation, and final failure at different interface fracture toughness values, i.e. $K_{Ic}^{Int} = 0.1, 0.6$ and 1.0 MPa$\sqrt{\text{m}}$, as well as for varying distances of $s = 0, 400, 800$ and 2400 nm. It is important to note that when $K_{Ic}^{Int} = 1.0$ MPa$\sqrt{\text{m}}$, $K_{Ic}^{Int} = K_{Ic}^{PVA}$. In Fig. 5a, during the crack initiation stage, microcracks appear at the MMT tips in the middle of the PVA film when the distance between the MMTs is 0–800 nm. Additionally, for $s = 2400$ nm, the first microcracks are also seen at the outer MMT tips, which are closer to the edges. For the thick PVA case, microcracks are only observed at the bottom two MMT tips, and as strain increases, microcracks are also observed at the upper tips. These findings validate the results presented in Fig. 4**D** indicating that as the K_{Ic}^{Int} and s increase, the COS increases simultaneously. The only exception for the cracking behavior occurs when the $K_{Ic}^{Int} = 1.0$ MPa$\sqrt{\text{m}}$ and $s = 400$ nm. In this case, a cohesive crack is immediately observed, followed by delamination damage. On the other hand, just before the cohesive crack initiates, the microscopic damage levels are noticed as ~0.14, and they are not considered as micro-cracks since the levels are less than 0.25. When s is increased, stress concentrations decrease at the tips, and this cohesive crack is not observed. Conversely, when the MMT tips are just touching each other ($s = 0$ nm), no cohesive crack is observed as there is no PVA material between the tips, unlike the s= 400 nm case, where stresses were concentrated at the tips.

Fig. 5B illustrates the stage of crack propagation. It is clear that as the

strain increases, the MMTs are pulled out from their tips when $K_{Ic}^{Int} = 0.1$ MPa$\sqrt{\text{m}}$. In addition, minimal delamination damage is visible between the PET substrate and PVA film when $s = 800$ nm. However, delamination damage is noticeable in other cases only at higher strain levels. It should be noted that delamination on the plot will be marked by a yellow circle or described below the damage. When the K_{Ic}^{Int} is increased to 0.6 MPa$\sqrt{\text{m}}$, pull-out damage is also observed at higher strain levels; however, these pull-outs combine two or five MMTs when s is between 400 nm and 2400 nm. Remarkably, all the MMTs are pulled out from the bottom to the top in the thick PVA when $s = 2400$ nm. In the case of the K_{Ic}^{Int} becomes equal to the K_{Ic}^{PVA}, the micro-cracks that originate at the MMT tips grow into cohesive cracks. This often results in delamination damage, especially in the $s = 400, 800$ and 2400 nm cases. However, a cohesive crack is not observed when the PVA film is thick, and microcracks will later evolve into that, as evident in the plot of the final failure stage. It is worth noting that the final failure is only established when the cohesive crack reaches the film's surface. In most of the propagation instances, the cracks have not yet reached the surface, except when $K_{Ic}^{Int} = 1.0$ MPa$\sqrt{\text{m}}$. In this case, micro-cracks abruptly transform into cohesive cracks, creating openings on the film surfaces.

In the final failure stage (Fig. 5**C**), the only observed damage mode when the K_{Ic}^{Int} is at its lowest value (0.1 MPa$\sqrt{\text{m}}$), is the pull-out damage of the MMTs as well as minor delaminations between the substrate and the film. Increasing the K_{Ic}^{Int} value to the level of 0.6 MPa$\sqrt{\text{m}}$, the final failures are still MMT pull-outs, but not individual pull-outs; instead, they are combinations of many or all fillers as evident in Fig. 5**C**. Surface openings are only seen either when the MMTs are just touching each other or when the $s = 2400$ nm. Surface opening at lower s has not been observed since the strain levels are not sufficiently high at this point. However, when the MMTs are just touching each other, opening mode becomes dominant. Increasing the K_{Ic}^{Int} value to the level of PVA matrix fracture toughness; the only final failure mode observed is cohesive cracks with delamination at the PET-PVA interface.

In summary, when the MMTs are perfectly bonded to the PVA matrix, they tend to fracture suddenly, leading to cohesive cracks and ultimately resulting in delamination damages shortly after the crack initiations at the tips of the MMTs, particularly the bottom ones. On the other hand, when the bonding forces between the PVA and MMT are weaker, the dominant type of damage is pull-out, and this type may eventually lead to cohesive crack formation. However, surface openings can still be observed in later stages after failure.

An alternative investigation for crack propagations and crack onset strains involves increasing the weight ratio of the MMTs, as shown in Fig. 6**A**. The weight ratios for each case are denoted in the columns below the figure. It is important to note that these weight ratios correspond to those in Fig. 6B, which illustrates the COS in a specific order. Additionally, the blocks in Fig. 6B, indicated by dotted (below) and solid lines (above), represent thin and thick layers, respectively. In Fig. 6, the distance between the MMTs remains fixed at $s = 200$ nm. In the initial scenario, the weight ratio remains at 30 %, consistent with the earlier instances. Subsequently, additional MMT fillers are incorporated between the current ones along the thickness direction using the MMT distributions from the 30 % case. This leads to weight ratios of 36 % and 41 % for the thin and thick PVA cases, respectively. Lastly, the weight ratio is increased to 70 % by adjusting the unit cell dimensions to $L = 11 \mu m$ and $W = 500$ nm. Thus, the distribution of MMTs resembles that of the 30 % case.

The crack onset strains of the above scenarios are plotted in Fig. 6**B** with varying K_{Ic}^{Int} from 0.1 to 1.0 MPa$\sqrt{\text{m}}$. The COS of both thin and thick PVA films are found to be similar, with thick PVA showing slightly larger COS values. Interestingly, when the weight ratio is increased with MMT insertions, as for the second case, there is a noticeable increase in COS, ranging between 22 % and 46 % for different K_{Ic}^{Int} values. Precisely, the increase in COS is calculated as 45.53 %, 29.11 %, 28.67 %, 22.35 %,

Fig. 6. Effect of weight ratios and insertions in the MMT arrangement on the COS and damage evolution behavior: (A) The MMTs distributed in thin (above) and thick (below) PVA films leading to different weight ratios. (B) COSs with varying K_{Ic}^{int} in both thin and thick PVA films (C) The PD simulation results on the damage initiation with different weight ratios and interfacial fracture toughness.

35.84 % for $K_{Ic}^{Int} = 0.1, 0.4, 0.6, 0.8$ and $1.0 \, \mathrm{MPa}\sqrt{\mathrm{m}}$, respectively. Typically, an increase in weight ratio would be expected to decrease the COS, however, the distribution of MMTs is altered with the insertions, which in turn changes the crack onset sites and increases COS accordingly. The stress concentrations become more pronounced at the MMT tips close to the right edges of the films, rather than at the mid-MMT tips.

This is because the insertions enhance the stiffness of the mid-regions compared to their counterparts without the insertions. Consequently, micro-cracks emerge at those sites as shown in Fig. 6C, followed by Figs. 7A and 7B. On the other hand, when the weight ratio is increased to 70 % with MMT distributions similar to the 30 % case, the COS decreases as expected, with values of 29.77 % and 27.95 % for $K_{Ic}^{Int} =$
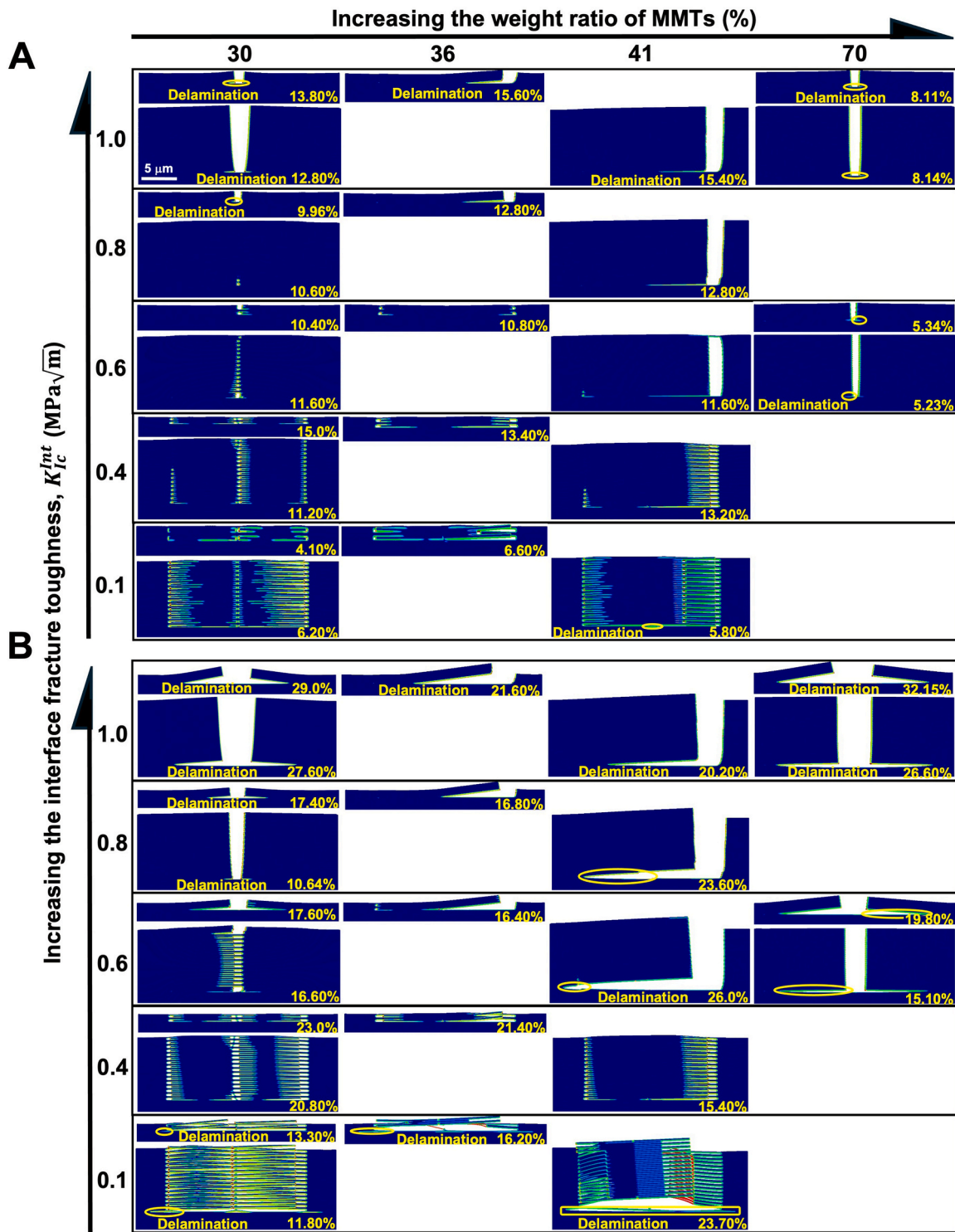
Fig. 7. The PD simulation results on the damage propagation and final failure as a function of different weight ratios and interfacial fracture toughness. The MMTs distributed in thin (above) and thick(below) PVA films in the (A) propagation and (B) final failure stage.

0.6 and 1.0 MPa$\sqrt{\text{m}}$, respectively. These findings closely match with the experimental results which verify decreasing COS with increasing weight ratio of MMT fillers. A more detailed discussion on this is provided in the next section. In Fig. 7, the peridynamic analyses for 70 % weight ratio of MMT fillers are completed with only the fracture toughness values of 0.6 and 1.0 MPa$\sqrt{\text{m}}$ since they are considered to be the cases which closely match with experimental results.

The interface fracture toughness values of 0.8 and 1.0 MPa$\sqrt{\text{m}}$ result

in the formation of small micro-cracks at the tips. These micro-cracks lead to cohesive cracks with sudden delamination, as shown in Fig. 7B. Only when the MMTs are inserted, as in the second scenario, the cohesive crack locations change. As explained earlier, the higher stiff regions help to alleviate stress concentrations in the mid-regions, causing this change. When the interface fracture toughness is decreased to 0.6 MPa$\sqrt{\text{m}}$, some cohesive cracks do not lead to delamination but propagate just at the bottom of the MMTs, while others cause

partial delamination at the higher strains. It is at this value that the balance between delamination and MMT pull-put damage begins. Further decreasing the value of K_{Ic}^{Int} results in the predominance of the MMT pull-out and delamination not related to cohesive cracks but observed at very high stresses due to shear displacement development between the PET substrate and PVA matrix.

4. Discussion on the combined results

Both COSs in the experimental and computational findings decrease as the MMT weight ratios increase from 30 % to 70 %. In experiments, the COS decreases by 40.63 %, while it decreases by 29.77 % and 27.95 % in the computational results for the interfacial fracture toughness of 0.6 and 1.0 MPa$\sqrt{\text{m}}$, respectively. It is important to note that various pre-existing discontinuities in the PVA matrix, including voids, cracks, and debonds, can influence COS. While all the computational analyses are carried out using pristine PVA, MMT, and PET materials, leading to crack initiations consistently occurring at the tips of the MMTs, the crack onset sites in the experiments can coincide with such discontinuities, which potentially decrease the COS. The lowest COS occurs when the distance between the MMTs, s, is less than 100 nm at all K_{Ic}^{Int} values and the minimum COS is 1.20 % with $K_{Ic}^{Int} = 0.1$ MPa$\sqrt{\text{m}}$. Increasing K_{Ic}^{Int} to 0.4 MPa$\sqrt{\text{m}}$, the minimum COS becomes 4.42 %. According to those results and considering the experimentally found value of COS 3.20 %, the K_{Ic}^{Int} should fall in between 0.27 and 0.29

MPa$\sqrt{\text{m}}$. However, based on the computational results, MMT pull-out is the only failure mode at or below the $K_{Ic}^{Int} = 0.6$ MPa$\sqrt{\text{m}}$. Referring back to the experimental findings for PET-30PVA, some MMT pull-outs occur on the film, but this is not the sole failure mode for this nanocomposite. The sudden occurrence of delamination triggered by cohesive cracks is also observed at early strains. This can only happen if the interfacial fracture toughness values are close to the PVA's toughness value. The PVA matrix fracture toughness is estimated to be 0.17 – 0.36 MPa$\sqrt{\text{m}}$ to represent the observed experimental COS values of PET-30PVA. The decrease in K_{Ic}^{PVA} can be attributed again to the pre-existing discontinuities in the PVA matrix and/or at the PVA and MMT interfaces. However, we assume the pristine PVA's fracture toughness to be 1.0 MPa$\sqrt{\text{m}}$, used in the previous studies, for the computational analyses.

When K_{Ic}^{Int} becomes less than 0.6 MPa$\sqrt{\text{m}}$, individual pull-outs are observed, leading to delamination at very later stages of the analysis. Fig. 8 shows the trend when the distance between the MMTs is interpreted as filler loading: the increased wt% (i.e. 53.20 %) accelerates the COS and the energy release rate is spent more on cohesive film cracking, while the decreased wt% (i.e. 38.37 %) delays the COS and the energy release rate is spent more on delamination from the substrate.

The earliest COS is observed in PET-70PVA in the experiments, consistent with the computational results. The experimental findings indicate a lack of delamination in the case of 70 % weight ratios of MMTs, attributed to two potential reasons. One possibility is that the interfacial fracture toughness is significantly lower than the PVA's
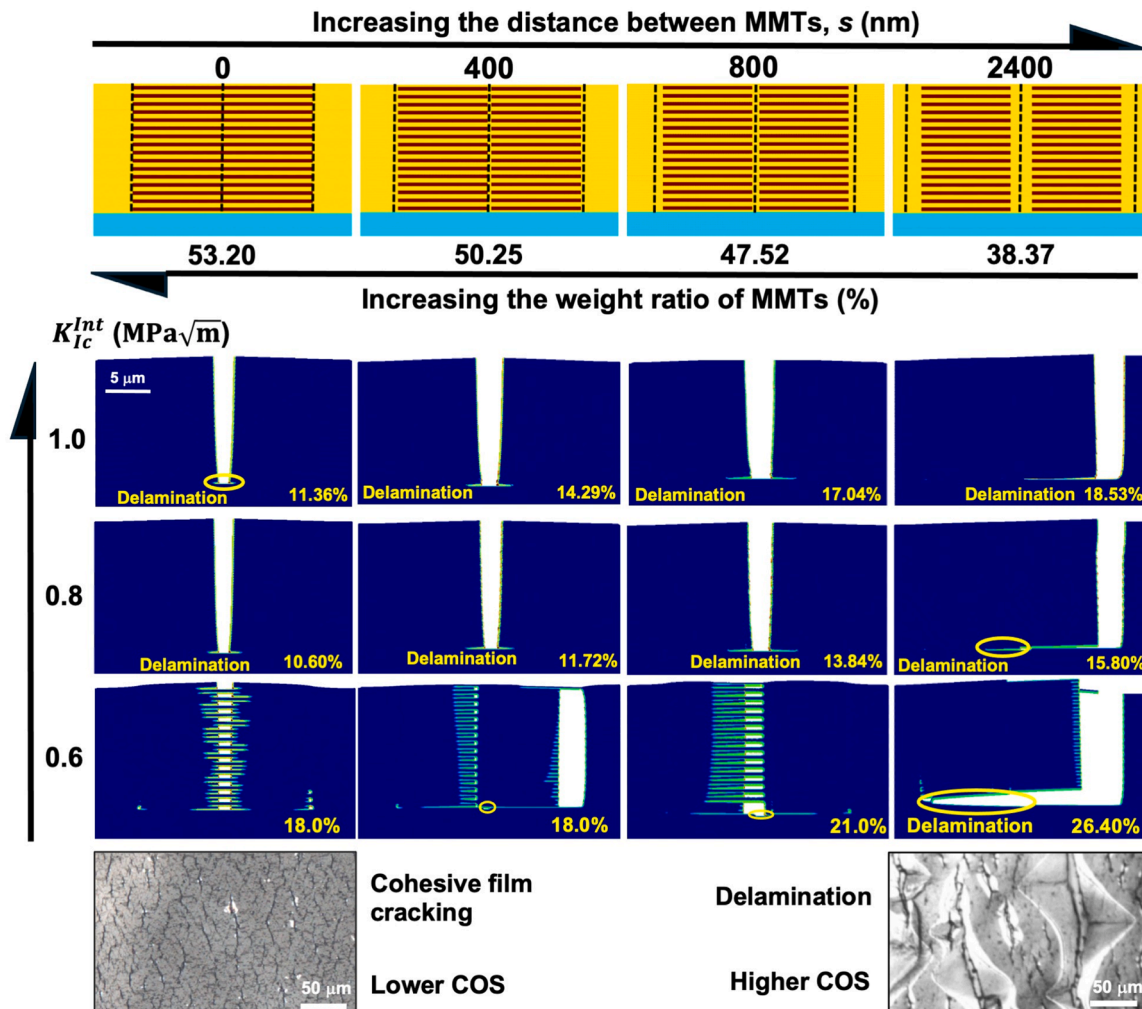

Fig. 8. Failure mode transition under varying weight ratios (from 53.20 % to 38.37 %) as the distance between MMTs increases observed in the PD simulation (top) and experiment (bottom).

toughness value, leading to the only failure mode being individual MMT pull-outs without delamination or only minor ones at higher strain levels. The computational analyses demonstrate this behavior when the K_{Ic}^{Int} value ranges from 0.1 to 0.4 MPa$\sqrt{m}$. Another contributing factor is the obstruction of crack propagations by MMTs. In the computational results of 70 % weight ratio of MMTs, the primary failure mode involves cohesive cracks with delamination (in contrast to the experimental observations) for the K_{Ic}^{Int} values of 0.6 and 1.0 MPa$\sqrt{m}$. These higher values of interface fracture toughness could also reveal local micro-crack propagations through the MMT interfaces in the form of pull-outs. However, due to the two-dimensional (2D) nature of the computational model, the pull-outs at higher K_{Ic}^{Int} values cannot be observed, as the model only provides a cross-sectional cut from the mid-region of cylindrical MMTs. This limitation leads to the dense distributions and rectangular representations of MMTs in the 2D model. Therefore, modeling the PET-70PVA film in 3D can better present the composite system, which is not considered in this study.

5. Conclusion

We introduce experimental findings on the fragmentation behavior of PVA matrix coated onto PET substrates with 30 %, 50 %, and 70 % MMT nanoflake fillers. Then, to understand the initiation, locations, and propagation of cracks, we carry out computational analyses for various scenarios involving the distribution of MMTs, interface fracture toughness values, as well as thin and thick PVA films. For damage analyses, the meshless PD theory and incorporated FE results are utilized to transfer displacements without cracks and predict initial strain values. The solution strategies presented significantly reduce solution times and substrate thickness by using classical continuum mechanics theory under plane strain conditions. By delving into solution strategies and exploring near interface elasticity modulus changes as well as critical stretch values to simulate the results, various scenarios are solved with the full results from crack initiation to final failure at crack saturation demonstrated in the **Section S4**. Upon reviewing the computational damage results alongside the experimental findings, the potential crack onset sites, crack propagation paths, crack arrests, and cohesive cracks leading to delamination have been identified. These findings provide valuable insights for the design of future thin film flexible electronics capable of withstanding damage up to 5 % strains. This can be further improved by carefully manipulating the weight ratios of MMTs and their distributions. Additionally, the presentation of moisture barrier testing gives us a glimpse into designing structures with enhanced moisture barrier capabilities. In the case of random distributions, the distances between the MMT fillers vary, as do the interface properties. Inserting MMT fillers into the mid-region of the PVA matrix could be considered an effect that disrupts the regular arrangements. It increases the rigidity, and the resultant crack locations and the COS values change. Random distributions will have the combination of such effects. The crucial point observed in the simulations is that the cracks emerge at the tip locations of bottom MMT fillers, which are close to the film-substrate interface. Cracks emerge at the tips of these chunks where the stiffness of the PVA matrix is less than that of other regions. Overall, this work opens the potential to be expanded to include the consideration of statistically representative random distributions of MMT fillers as well as a three-dimensional modeling scheme, but such endeavors are left for future research.

6. Materials and methods

MMT/PVA-PET processing: The nanocomposite films are made via layer-by-layer dipping of a 131 μm-thick PET substrate into MMT (Na$^+$ cloisite (NaMMT) from BYK)/polyvinyl alcohol (PVA, Sigma Aldrich)/deionized water solution. The MMT and PVA construct 1.5 % of the overall nanocomposite by volume, with the DI water making up the other 98.5 %. The MMT is dispersed with a stir bar for approximately 15 minutes on a 130°C hot plate, followed by ultrasonication for 30 minutes, before being added to the PVA dispersion at room temperature and stirred for 20 minutes. The complete solution is ultrasonicated again for 30 minutes and stirred continuously throughout the dipping procedure. Each dipping is followed by drying in an oven at 60°C for minimum 30 minutes, at which point the substrate is rotated 180° to allow for even coating for the same duration. The film remains vertical to allow for the gravitationally assisted nanoplate alignment.

Plasma treatment: Some samples are tested at room temperature with a plasma gun (Plasma Wand from Plasma Etch, Inc) between layers during the dipping process. The plasma treatment procedure involves placing a dry sample on a flat surface on a clean Kimtech wipe in the fume hood and submitting each side to oxygen plasma for 30 seconds before dipping it in the nanocomposite dispersion again. This step was consistently carried out prior to applying each new film layer.

***in situ* microscopy mechanical test:** Mechanical properties are tested with a modular force stage (Linkam MFS). The samples are prepared to a size of 4 mm wide and 40 mm long, clamped and pulled under uniaxial tensile strain until the failure at loading rates of 50 μm/s. Applied force and extension are recorded along with *in situ* optical images (Nikon's Eclipse LV100N POL, polarized light microscope). Crack onset strains and crack densities are determined from the recorded videos. The experimentally observed crack onset strain is the applied tensile strain when the crack growth is first observed, and the crack density is the number of cracks over the observation area (unit of mm^{-1}), through the loading direction. Process-induced residual stresses can occur in the film, and the applied strain can be updated in such cases by including the residual strain ($\varepsilon_{applied} + \varepsilon_{residual}$) in the stress calculation.

Cross-section imaging: A cross-sectional image of the flake composite film is taken with a Teneo scanning electron microscope. The sample is cut on one end and then torn while submerged in liquid nitrogen, preserving the layers in the cold environment, followed by 2 nm of gold sputtering.

Transparency test: A UV-Vis spectrometer (Agilent Cary 60 UV-Vis spectrophotometer) is used to measure the wavelengths passing through bare PET and MMT/PVA-PET samples with 10 and 30 dipping layers with and without the plasma treatment.

Barrier performance test: Water vapor transmission rates are measured through a permeation analyzer (Amatek MOCON, Aquatran 3) following the ASTM 3299 standard. This setup involves placing the film between two gas chambers, dry and wet sides. The relative humidity and temperature of the wet chamber are set to 100 % RH and 37 °C. In contrast, the dry chamber flows through nitrogen-carrying permeated water vapor molecules to an electrolytic sensor that calculates the transmission rate in the unit of g/m^2/day. This permeation analyzer's detection limit is 5 g/m^2/day; therefore previously tested WVTR value of PET is used, i.e. 6 g/m^2/day. [85]

All samples are created, characterized, and tested by ensuring sufficient numbers and times to extract the standard deviations and average values to draw statistically solid data and trends.

CRediT authorship contribution statement

Rebecca Villanueva: Writing – original draft, Visualization, Validation, Investigation, Formal analysis, Data curation. **Cagan Diyaroglu:** Writing – original draft, Visualization, Validation, Methodology, Investigation, Formal analysis, Data curation, Conceptualization. **Selda Oterkus:** Writing – review & editing, Supervision, Methodology. **Umar Raza:** Validation, Investigation, Data curation. **Erkan Oterkus:** Writing – review & editing, Supervision, Methodology. **Kyungjin Kim:** Writing – review & editing, Writing – original draft, Visualization, Validation, Supervision, Resources, Project administration, Methodology, Investigation, Funding acquisition, Conceptualization.

Declaration of Competing Interest

The authors declare that they have no known competing financial interests or personal relationships that could have appeared to influence the work reported in this paper.

Acknowledgements

Appendix A. Supporting information

Supplementary data associated with this article can be found in the online version at doi:10.1016/j.eml.2024.102268.

Data availability

Data will be made available on request.

References

[1] Polymer Nanocomposites Market Share and Statistics - 2028. *Global Market Insights Inc.*

[2] K. Kim, et al., Optimizing crack onset strain for silicon nitride/fluoropolymer nanolaminate barrier films, ACS Appl. Nano Mater. 2 (2019) 2525–2532.

[3] P. Das, et al., Nacre-mimetics with synthetic nanoclays to ultrahigh aspect ratios, Nat. Commun. 6 (2015) 5967.

[4] J. Yu, et al., High gas barrier coating using non-toxic nanosheet dispersions for flexible food packaging film, Nat. Commun. 10 (2019) 2398.

[5] Y. Li, et al., Encapsulation of Fe_3O_4 between copper nanorod and thin TiO_2 film by ALD for lithium-ion capacitors, ACS Appl. Mater. Interfaces 11 (2019) 19115–19122.

[6] P.-G. Ren, et al., Ultrahigh gas barrier poly (vinyl alcohol) nanocomposite film filled with congregated and oriented Fe_3O_4 @GO sheets induced by magnetic-field, Compos. Part Appl. Sci. Manuf. 97 (2017) 1–9.

[7] C. Sanchez, B. Julián, P. Belleville, M. Popall, Applications of hybrid organic–inorganic nanocomposites. J. Mater. Chem. 15 (2005) 3559.

[8] K. Kim, et al., Extended barrier lifetime of partially cracked organic/inorganic multilayers for compliant implantable electronics, Small 17 (2021) 2103039.

[9] M. Dumont, J. Reyna-Valencia, A. Emond, J. -P, M. Bousmina, Barrier properties of polypropylene/organoclay nanocomposites, J. Appl. Polym. Sci. 103 (2007) 618–625.

[10] S. Park, et al., Improvements in barrier properties of poly(lactic acid) films coated with chitosan or chitosan/clay nanocomposite, J. Appl. Polym. Sci. 125 (2012).

[11] F. Ding, et al., Biomimetic nanocoatings with exceptional mechanical, barrier, and flame-retardant properties from large-scale one-step coassembly, Sci. Adv. 3 (2017) e1701212.

[12] S. Yue, et al., Polyvinyl alcohol/montmorillonite nanocomposite coated biodegradable films with outstanding barrier properties, ES Mater. Manuf. (2023), https://doi.org/10.30919/esmm5f834.

[13] A. Giannakas, K. Grigoriadi, A. Leontiou, N.-M. Barkoula, A. Ladavos, Preparation, characterization, mechanical and barrier properties investigation of chitosan–clay nanocomposites, Carbohydr. Polym. 108 (2014) 103–111.

[14] A. Kalendova, D. Merinska, J.F. Gerard, M. Slouf, Polymer/clay nanocomposites and their gas barrier properties, Polym. Compos. 34 (2013) 1418–1424.

[15] H.L. Calambas, A. Fonseca, D. Adames, Y. Aguirre-Loredo, C. Caicedo, Physical-mechanical behavior and water-barrier properties of biopolymers-clay nanocomposites, Molecules 26 (2021) 6734.

[16] H. Le Ferrand, F. Bouville, T.P. Niebel, A.R. Studart, Magnetically assisted slip casting of bioinspired heterogeneous composites, Nat. Mater. 14 (2015) 1172–1179.

[17] T. Akter, W.S. Kim, Reversibly stretchable transparent conductive coatings of spray-deposited silver nanowires, ACS Appl. Mater. Interfaces 4 (2012) 1855–1859.

[18] A.M. LaChance, et al., Spin coating for forming thin composite coatings of montmorillonite and poly(vinyl alcohol), Ind. Eng. Chem. Res. 61 (2022) 4168–4177.

[19] A.M. LaChance, et al., Doctor-Blade-Assisted Casting for Forming Thin Composite Coatings of Montmorillonite and Poly(vinyl alcohol), Ind. Eng. Chem. Res. 61 (2022) 3766–3774.

[20] M.A. Priolo, D. Gamboa, J.C. Grunlan, Transparent clay−polymer nano brick wall assemblies with tailorable oxygen barrier. ACS Appl. Mater. Interfaces 2 (2010) 312–320.

[21] M.A. Priolo, D. Gamboa, K.M. Holder, J.C. Grunlan, Super gas barrier of transparent polymer−clay multilayer ultrathin films, Nano Lett. 10 (2010) 4970–4974.

[22] Y. Song, et al., Edge charge neutralization of clay for improved oxygen gas barrier in multilayer nanobrick wall thin films, ACS Appl. Mater. Interfaces 8 (2016) 34784–34790.

[23] J. Liu, et al., Ultra-transparent nanostructured coatings via flow-induced one-step coassembly, Nano Mater. Sci. 4 (2022) 97–103.

[24] M.A. Priolo, K.M. Holder, T. Guin, J.C. Grunlan, Recent advances in gas barrier thin films via layer-by-layer assembly of polymers and platelets, Macromol. Rapid Commun. 36 (2015) 866–879.

[25] Y. Zhou, et al., Nanofluidic energy conversion and molecular separation through highly stable clay-based membranes, J. Mater. Chem. A 7 (2019) 14089–14096.

[26] J. Peng, Q. Cheng, Smart nacre-inspired nanocomposites. ChemPhysChem 19 (2018) 1980–1986.

[27] B. Tan, N.L. Thomas, A review of the water barrier properties of polymer/clay and polymer/graphene nanocomposites, J. Membr. Sci. 514 (2016) 595–612.

[28] J. Zhu, J. Breu, H. Hou, A. Greiner, S. Agarwal, Gradient-structured nonflammable flexible polymer membranes, ACS Appl. Mater. Interfaces 11 (2019) 11876–11883.

[29] A. Fahami, J. Lee, S. Lazar, J.C. Grunlan, Mica-based multilayer nanocoating as a highly effective flame retardant and smoke suppressant, ACS Appl. Mater. Interfaces 12 (2020) 19938–19943.

[30] P. Das, H. Thomas, M. Moeller, A. Walther, Large-scale, thick, self-assembled, nacre-mimetic brick-walls as fire barrier coatings on textiles, Sci. Rep. 7 (2017) 39910.

[31] W. Xu, et al., Nacre-inspired tunable strain sensor with synergistic interfacial interaction for sign language interpretation, Nano Energy 90 (2021) 106606.

[32] M. Laipan, et al., Layered intercalation compounds: mechanisms, new methodologies, and advanced applications, Prog. Mater. Sci. 109 (2020) 100631.

[33] S. Wan, J. Peng, L. Jiang, Q. Cheng, Bioinspired graphene-based nanocomposites and their application in flexible energy devices. Adv. Mater. 28 (2016) 7862–7898.

[34] A.K. Singh, et al., Effects of particle inclusions on cracking in ultrathin barrier films, Thin Solid Films 714 (2020) 138387.

[35] K. Kim, O.N. Pierron, S. Graham, Atomic layer deposited Al2O3 capping layer effect on environmentally assisted cracking in SiNx barrier films, J. Appl. Phys. 125 (2019) 045301.

[36] M.H. Han, et al., Surface modification for adhesion enhancement of PET-laminated steel using atmospheric pressure plasma, Surf. Coat. Technol. 201 (2007) 4948–4952.

[37] C.J. Wohl, M.A. Belcher, S. Ghose, J.W. Connell, Modification of the surface properties of polyimide films using polyhedral oligomeric silsesquioxane deposition and oxygen plasma exposure, Appl. Surf. Sci. 255 (2009) 8135–8144.

[38] W. Huang, S. Zeng, J. Liu, L. Sun, Bi-axially oriented polystyrene/montmorillonite nanocomposite films, RSC Adv. 5 (2015) 58191–58198.

[39] K. Kim, et al., Environmentally assisted cracking in silicon nitride barrier films on poly(ethylene terephthalate) substrates, ACS Appl. Mater. Interfaces 8 (2016) 27169–27178.

[40] K. Kim, S. Graham, O.N. Pierron, Note: a single specimen channel crack growth technique applied to brittle thin films on polymer substrates, Rev. Sci. Instrum. 88 (2017).

[41] K. Kim, H. Luo, T. Zhu, O.N. Pierron, S. Graham, Influence of polymer substrate damage on the time dependent cracking of SiNx barrier films. Sci. Rep. 8 (2018).

[42] K.M. Holder, et al., Stretchable gas barrier achieved with partially hydrogen-bonded multilayer nanocoating. Macromol. Rapid Commun. 35 (2014) 960–964.

[43] C. Diyaroglu, M.T.M. Anaei, K. Kim, A finite element framework on water vapor transmission rates by pinhole damages in inorganic ultrabarriers for flexible electronics, App. Sur. Sci 659 (2024) 159870.

[44] M. Mariello, K. Kim, K. Wu, S.P. Lacour, Y. Leterrier, Recent advances in encapsulation of flexible bioelectronic implants: materials, technologies, and characterization methods, Adv. Mater. 34 (2022) 2201129.

[45] V. Zardetto, T.M. Brown, A. Reale, A. Di Carlo, Substrates for flexible electronics: a practical investigation on the electrical, film flexibility, optical, temperature, and solvent resistance properties, J. Polym. Sci. Part B Polym. Phys. 49 (2011) 638–648.

[46] R.D. Rodriguez, et al., Ultra-Robust flexible electronics by laser-driven polymer-nanomaterials integration, Adv. Funct. Mater. 31 (2021).

[47] C. Kathe, et al., The neurons that restore walking after paralysis, Nature 611 (2022) 540–547.

[48] C. Kathe, et al., Wireless closed-loop optogenetics across the entire dorsoventral spinal cord in mice, Nat. Biotechnol. 40 (2022) 198–208.

[49] F. Michoud, et al., Epineural optogenetic activation of nociceptors initiates and amplifies inflammation, Nat. Biotechnol. 39 (2021) 179–185.

[50] S.-H. Jen, J.A. Bertrand, S.M. George, Critical tensile and compressive strains for cracking of Al2O3 films grown by atomic layer deposition, J. Appl. Phys. 109 (2011) 084305.

[51] Y. Leterrier, Durability of nanosized oxygen-barrier coatings on polymers, Prog. Mater. Sci. 48 (2003) 1–55.

[52] J. Lewis, Material challenge for flexible organic devices, Mater. Today 9 (2006) 38–45.

[53] D.-H. Kim, et al., Epidermal electronics, Science 333 (2011) 838–843.

[54] J.A. Fan, et al., Fractal design concepts for stretchable electronics, Nat. Commun. 5 (2014).

[55] T. Widlund, S. Yang, Y.-Y. Hsu, N. Lu, Stretchability and compliance of freestanding serpentine-shaped ribbons, Int. J. Solids Struct. 51 (2014) 4026–4037.

[56] M. Niemiec, K. Kim, Lifetime engineering of bioelectronic implants with mechanically reliable thin film encapsulations, Prog. Biomed. Eng. 6 (2024) 012001.

[57] J.J. Vlassak, Channel cracking in thin films on substrates of finite thickness, Int. J. Fract. 119/120 (2003) 299–323.

[58] X. Li, et al., Micro/nanoscale mechanical characterization and in situ observation of cracking of laminated Si3N4/BN composites, Mater. Sci. Eng. C. 28 (2008) 1501–1508.

[59] M. Morits, et al., Toughness and fracture properties in nacre-mimetic clay/polymer nanocomposites. Adv. Funct. Mater. 27 (2017) 1605378.

[60] J. Wang, Q. Cheng, L. Lin, L. Jiang, Synergistic toughening of bioinspired Poly (vinyl alcohol)–clay–nanofibrillar cellulose artificial nacre. ACS Nano 8 (2014) 2739–2745.

[61] J. Peng, A.P. Tomsia, L. Jiang, B.Z. Tang, Q. Cheng, Stiff and tough PDMS-MMT layered nanocomposites visualized by AIE luminogens, Nat. Commun. 12 (2021) 4539.

[62] J. Wang, Q. Cheng, Z. Tang, Layered nanocomposites inspired by the structure and mechanical properties of nacre, Chem. Soc. Rev. 41 (2012) 1111–1129.

[63] I. Corni, et al., A review of experimental techniques to produce a nacre-like structure, Bioinspir. Biomim. 7 (2012) 031001.

[64] L.J. Bonderer, A.R. Studart, L.J. Gauckler, Bioinspired Design and Assembly of Platelet Reinforced Polymer Films, Science 319 (2008) 1069–1073.

[65] G. Ongaro, R. Bertani, U. Galvanetto, A. Pontefisso, M. Zaccariotto, A multiscale peridynamic framework for modelling mechanical properties of polymer-based nanocomposites, Eng. Fract. Mech. 274 (2022) 108751.

[66] W.B. Lawrimore, B. Paliwal, M.Q. Chandler, K.L. Johnson, M.F. Horstemeyer, Hierarchical multiscale modeling of polyvinyl alcohol/montmorillonite nanocomposites, Polymer 99 (2016) 386–398.

[67] S. Nayak, R. Ravinder, N.M.A. Krishnan, S. Das, A peridynamics-based micromechanical modeling approach for random heterogeneous structural materials, Materials 13 (2020) 1298.

[68] F. Baber, et al., Microstructural exploration of a carbon nanotube yarn reinforced composite using a peridynamic approach, J. Compos. Mater. 56 (2022) 861–876.

[69] A. Jenabidehkordi, R. Abadi, T. Rabczuk, Computational modeling of meso-scale fracture in polymer matrix composites employing peridynamics, Compos. Struct. 253 (2020) 112740.

[70] E. Madenci, E. Oterkus, Damage Prediction. in *Peridynamic Theory and Its Applications*, Springer New York, New York, NY, 2014, pp. 115–124, https://doi.org/10.1007/978-1-4614-8465-3_6.

[71] Silling, S.A., Gerstle, W.H. & Sau, N. *Peridynamic Modeling of Plain and Reinforced Concrete Structures*. (2005).

[72] Diyaroglu, C. Peridynamics and its applications in marine structures. (Glasgow, UK, 2016).

[73] Matsui, K., Hosoi, K., Feng, B., Yoshida, H. & Ikuhara, Y. Ultrahigh toughness polycrystalline ceramics without fading of strength. Preprint at https://doi.org/10.48550/ARXIV.2112.14372 (2021).

[74] Oterkus, S. Peridynamics for the solution of multiphysics problems. (University of Arizona, Tucson, AZ, 2015).

[75] B. Yeom, S. Kim, J. Cho, J. Hahn, K. Char, Effect of interfacial adhesion on the mechanical properties of organic/inorganic hybrid nanolaminates, J. Adhes. 82 (2006) 447–468.

[76] T. Ye, Z. Suo, A.G. Evans, Thin film cracking and the roles of substrate and interface, Int. J. Solids Struct. 29 (1992) 2639–2648.

[77] Y. Leterrier, L. Boogh, J. Andersons, J.-A.E. M?nson, Adhesion of silicon oxide layers on poly(ethylene terephthalate). I: effect of substrate properties on coating's fragmentation process, J. Polym. Sci. Part B Polym. Phys. 35 (1997) 1449–1461.

[78] N. Jain, V.K. Singh, S. Chauhan, A review on mechanical and water absorption properties of polyvinyl alcohol based composites/films, J. Mech. Behav. Mater. 26 (2017) 213–222.

[79] O.L. Manevitch, G.C. Rutledge, Elastic properties of a single lamella of montmorillonite by molecular dynamics simulation, J. Phys. Chem. B 108 (2004) 1428–1435.

[80] Mixed Mode Cracking in Layered Materials, Advances in Applied Mechanics, Elsevier, 1991, pp. 63–191, https://doi.org/10.1016/s0065-2156(08)70164-9.

[81] C. Liao, et al., Flexible organic electronics in biology: materials and devices, Adv. Mater. 27 (2015) 7493–7527.

[82] G. Findenig, et al., Creating water vapor barrier coatings from hydrophilic components, ACS Appl. Mater. Interfaces 4 (2012) 3199–3206.

[83] U. Raza, M. Niemiec, K. Kim, Polyisobutylene encapsulated PEDOT: Pss electrode honeycomb skeleton electrolyte for moisture resistant electro-ionic soft artificial muscles, Adv. Mater. Technol. 9 (2024).

[84] Kilic, B. Peridynamic theory for progressive failure prediction in homogeneous and heterogeneous materials. (The University of Arizona, Tucson, AZ, 2008).

[85] S. Buchwalder, F. Bourgeois, J.J.D. Leon, A. Hogg, J. Burger, Parylene-AlOx stacks for improved 3D encapsulation solutions, Coatings 13 (2023) 1942.